JGR Planets

RESEARCH ARTICLE
10.1029/2022JE007612

Special Section:
The Mars Perseverance Rover Jezero Crater Floor Campaign

Mineralogy, Morphology, and Emplacement History of the Maaz Formation on the Jezero Crater Floor From Orbital and Rover Observations

Briony Horgan[1], Arya Udry[2], Melissa Rice[3], Sanna Alwmark[4,5], Hans E. F. Amundsen[6], James F. Bell III[7], Larry Crumpler[8], Brad Garczynski[1], Jeff Johnson[9], Kjartan Kinch[5], Lucia Mandon[10], Marco Merusi[5], Chase Million[11], Jorge I. Núñez[9], Patrick Russell[12], Justin I. Simon[13], Michael St. Clair[11], Kathryn M. Stack[14], Alicia Vaughan[15], Brittan Wogsland[16], Andrew Annex[17,18], Andreas Bechtold[19,20], Tor Berger[6], Olivier Beyssac[21], Adrian Brown[22], Ed Cloutis[23], Barbara A. Cohen[24], Sarah Fagents[25], Linda Kah[16], Ken Farley[17], David Flannery[26], Sanjeev Gupta[27], Svein-Erik Hamran[6], Yang Liu[14], Gerhard Paar[28], Cathy Quantin-Nataf[29], Nicolas Randazzo[30], Eleni Ravanis[25], Steven Sholes[14], David Shuster[31], Vivian Sun[14], Christian Tate[32], Nick Tosca[33], Meenakshi Wadhwa[7], and Roger C. Wiens[1]

[1]Department of Earth, Atmospheric, and Planetary Sciences, Purdue University, West Lafayette, IN, USA, [2]Department of Geosciences, University of Nevada Las Vegas, Las Vegas, NV, USA, [3]Western Washington University, Bellingham, WA, USA, [4]Department of Geology, Lund University, Lund, Sweden, [5]Niels Bohr Institute, University of Copenhagen, Copenhagen, Denmark, [6]Center for Space Sensors and Systems (CENSSS), University of Oslo, Oslo, Norway, [7]School of Earth and Space Exploration, Arizona State University, Tempe, AZ, USA, [8]New Mexico Museum of Natural History and Science, Albuquerque, NM, USA, [9]Johns Hopkins University Applied Physics Laboratory, Laurel, MD, USA, [10]LESIA, Observatoire de Paris, Université PSL, CNRS, Sorbonne Université, Université de Paris, Meudon, France, [11]Million Concepts LLC, Louisville, KY, USA, [12]Department EPSS, University of California, Los Angeles, Los Angeles, CA, USA, [13]Center for Isotope Cosmochemistry and Geochronology, Astromaterials Research and Exploration Science, NASA Johnson Space Center, Houston, TX, USA, [14]Jet Propulsion Laboratory, California Institute of Technology, Pasadena, CA, USA, [15]Apogee Engineering, LLC, Flagstaff, AZ, USA, [16]Department of Earth and Planetary Sciences, University of Tennessee, Knoxville, TN, USA, [17]Division of Geological and Planetary Sciences, California Institute of Technology, Pasadena, CA, USA, [18]Morton K. Blaustein Department of Earth & Planetary Sciences, Johns Hopkins University, Baltimore, MD, USA, [19]Department of Lithospheric Research, University of Vienna, Vienna, Austria, [20]Austrian Academy of Sciences, Vienna, Austria, [21]Institut de Minéralogie de Physique des Matériaux et de Cosmochimie, CNRS, Sorbonne Université, Muséum National d'Histoire Naturelle, Paris, France, [22]Plancius Reseach LLC, Severna Park, MD, USA, [23]Centre for Terrestrial and Planetary Exploration, University of Winnipeg, Winnipeg, MB, Canada, [24]NASA Goddard Space Flight Center, Greenbelt, MD, USA, [25]Hawai'i Institute of Geophysics and Planetology, University of Hawai'i at Mānoa, Honolulu, HI, USA, [26]Queensland University of Technology, Brisbane, QLD, Australia, [27]Department of Earth Science and Engineering, Imperial College London, London, UK, [28]Joanneum Research, Institute for Information and Communication Technologies, Graz, Austria, [29]Laboratoire de Géologie de Lyon: Terre, Planètes, Environnement, Université de Lyon, Université Claude Bernard Lyon1, Ecole Normale Supérieure de Lyon, Université Jean Monnet Saint Etienne, CNRS, Villeurbanne, France, [30]Department of Earth and Atmospheric Sciences, University of Alberta, Edmonton, AB, Canada, [31]Department of Earth and Planetary Science, University of California, Berkeley, Berkeley, CA, USA, [32]Department of Astronomy, Cornell University, Ithaca, NY, USA, [33]Department of Earth Sciences, University of Cambridge, Cambridge, UK

Key Points:

- The Maaz formation is a series of pyroxene- and plagioclase-dominated lava flows on the Jezero crater floor with variable morphologies
- Significant erosion and tectonism occurred during at least one flow hiatus, suggesting emplacement over an extended period of time
- The crystallization ages of Maaz formation samples will help constrain the timing of delta activity and the global cratering chronology

Supporting Information:

Supporting Information may be found in the online version of this article.

Correspondence to:
B. Horgan,
briony@purdue.edu

Citation:
Horgan, B., Udry, A., Rice, M., Alwmark, S., Amundsen, H. E. F., Bell, J. F. III, et al. (2023). Mineralogy, morphology, and emplacement history of the Maaz formation on the Jezero crater floor from orbital and rover observations. *Journal of Geophysical Research: Planets*, *128*, e2022JE007612. https://doi.org/10.1029/2022JE007612

Received 7 OCT 2022
Accepted 22 JUN 2023

Abstract The first samples collected by the Perseverance rover on the Mars 2020 mission were from the Maaz formation, a lava plain that covers most of the floor of Jezero crater. Laboratory analysis of these samples back on Earth would provide important constraints on the petrologic history, aqueous processes, and timing of key events in Jezero crater. However, interpreting these samples requires a detailed understanding of the emplacement and modification history of the Maaz formation. Here we synthesize rover and orbital remote sensing data to link outcrop-scale interpretations to the broader history of the crater, including Mastcam-Z mosaics and multispectral images, SuperCam chemistry and reflectance point spectra, Radar Imager for Mars' subsurface eXperiment ground penetrating radar, and orbital hyperspectral reflectance and high-resolution images. We show that the Maaz formation is composed of a series of distinct members corresponding to basaltic to basaltic-andesite lava flows. The members exhibit variable spectral signatures dominated by high-Ca pyroxene, Fe-bearing feldspar, and hematite, which can be tied directly to igneous grains and altered matrix in abrasion patches. Spectral variations correlate with morphological variations, from recessive layers that produce a regolith lag in lower Maaz, to weathered polygonally fractured paleosurfaces and crater-retaining massive blocky hummocks in upper Maaz. The Maaz members were likely separated by one or more extended periods

of time, and were subjected to variable erosion, burial, exhumation, weathering, and tectonic modification. The two unique samples from the Maaz formation are representative of this diversity, and together will provide an important geochronological framework for the history of Jezero crater.

Plain Language Summary The Perseverance rover on the Mars 2020 mission is collecting samples from Jezero crater for potential return to Earth via Mars Sample Return, and the first samples collected by the rover were from the Maaz formation, a lava plain that covers much of the crater floor. These igneous samples can be used to date when the lavas crystallized and to better understand their subsequent interactions with water, both of which will be important for reconstructing the history of habitable environments in Jezero crater. In this study we use images and reflectance spectra from the rover and orbiters, along with ground penetrating radar from the rover, to determine the history of the Maaz formation lavas. We find evidence for significant erosion and weathering in between successive flows, suggesting that they were emplaced over a long period of time. Some of the lavas underlie the Jezero delta, and so their age will provide limits on the timing of lake activity in Jezero crater, while others retain craters, so their age will help to better understand crater density-based age estimates for surfaces across Mars.

1. Introduction

The Perseverance rover on the Mars 2020 mission is collecting samples from Jezero crater, a Noachian impact crater that has experienced a complex history of igneous, aqueous, and aeolian processes (Farley et al., 2020), for potential return to Earth. Two of the four unique rock samples acquired by Perseverance on the Jezero crater floor were extracted from the Maaz formation, which from orbit corresponds to a rough unit with lobate margins that appears to embay local topography (Figure 1). Morphologic and petrologic observations of the Maaz formation by Perseverance are most consistent with a series of lava flows (Alwmark et al., 2023; Crumpler et al., 2023; Farley et al., 2022; Udry et al., 2022), confirming some hypotheses based on orbital data that the unit is igneous in origin (Goudge et al., 2015; Horgan et al., 2020a; Schon et al., 2012; Sun & Stack, 2020).

The Maaz formation ("Máaz" is the Navajo name for Mars) provides an important stratigraphic and geochronological link between other major geologic units in Jezero crater. The Maaz formation overlies the Seitah formation ("Séítah" is Navajo for "amidst the sands"), which is a layered and eroded landscape of ridges and sand that is interpreted as an olivine-dominated cumulate likely originating in a thick lava flow or lava lake that once filled the crater floor (Liu et al., 2022). The western delta and other sedimentary remnants in Jezero crater appear to overlie the Maaz formation (Holm-Alwmark et al., 2021), suggesting that some or all lacustrine activity post-dated emplacement of crater floor lavas. Geochronological analyses of these samples back on Earth may thus provide critical constraints on the timing of events in Jezero crater, including emplacement of the crater floor as well as potentially the onset of lake activity (Simon et al., 2023). Crater densities on the Maaz formation may also provide important constraints on interpretations of the global martian crater chronology, if the surface's erosional, burial, and exhumation history can be constrained (Quantin-Nataf et al., 2023). However, additional geologic context from rover and orbital data sets is needed to understand how the Maaz formation fits into the regional history.

In this paper, we tie in situ observations from Perseverance to orbital data to understand the emplacement history and geochronological significance of the Maaz formation. We seek to understand the relationships between stratigraphic members in outcrop and how these members relate to morphologies and spectral properties observed from orbit, in order to develop a framework for the emplacement history of crater floor rocks and their relationship to the delta. We investigate the compositional and morphological diversity of stratigraphic members within the Maaz formation as observed by Perseverance using Mastcamera-Zoom (Mastcam-Z) multispectral images, SuperCam reflectance spectra and elemental chemistry, as well as Radar Imager for Mars' Subsurface Exploration (RIMFAX) ground penetrating radar (GPR), and compare these results to orbital spectral data from Compact Reconnaissance Imaging Spectrometer for Mars (CRISM) and orbital images from High Resolution Science Imaging Experiment (HiRISE).

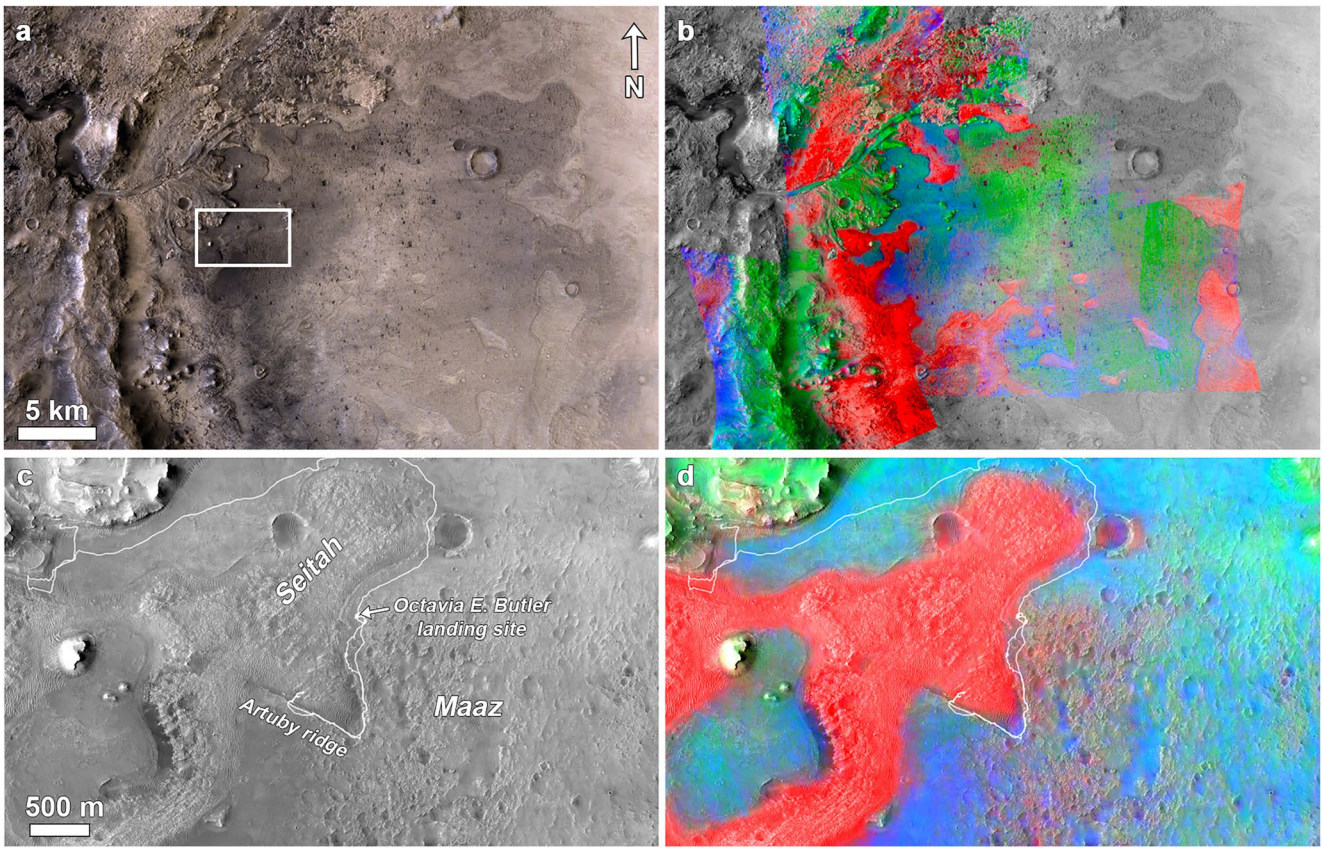

Figure 1. Overview of Jezero crater floor. (a) Context camera (CTX) mosaic (Fergason et al., 2020) colorized with stretched High-Resolution Stereo Camera images showing lobate margins of Maaz formation (map centered near 77.53°E, 18.44°N). (b) Compact Reconnaissance Imaging Spectrometer for Mars (CRISM) mafic parameter combination (Horgan et al., 2020a) over CTX mosaic, where red, green, and blue (RGB) indicate olivine-like, orthopyroxene-like, and clinopyroxene spectral signatures. The Maaz formation is dominated by pyroxene spectral signatures, in contrast to the olivine signatures of the Seitah formation. (c, d) Zoom in on High Resolution Science Imaging Experiment (HiRISE) mosaic (Fergason et al., 2020) and CRISM RGB combination over HiRISE in the region of Perseverance's traverse, which shows more diversity at local scales in Maaz.

2. Methods

2.1. Mastcam-Z

Mastcam-Z (Bell et al., 2021) is a pair of mast-mounted cameras on the Perseverance rover that have adjustable focal lengths equipped with charge-coupled device (CCD) detectors with bonded Bayer-pattern broadband filters at red/green/blue wavelengths (RGB; 630/544/480 nm). Each camera is also equipped with a filter wheel with additional narrowband filters, enabling multispectral imaging across the visible/near-infrared (VNIR, 442–1,022 nm) at 14 unique wavelengths (Hayes et al., 2021). Mastcam-Z images are calibrated to radiance factor (I/F; where I is the scene radiance and πF is the solar irradiance) using near-simultaneous observations of a calibration target mounted on the rover deck (Kinch et al., 2020; Merusi et al., 2022) and pre-flight calibration coefficients (Hayes et al., 2021). Spectra are then converted to relative reflectance (R^*) by dividing by the cosine of the solar incidence angle.

Mastcam-Z acquired >300 multispectral images as well as ~300 landscape mosaics during the crater floor campaign (sols 0–380) and the following "rapid traverse" over the crater floor to the delta (sols 381–409, Sun et al., 2023). Spectral diversity was assessed in multispectral images using enhanced-color images, decorrelation stretches, and spectral parameter maps (Rice et al., 2022a; Rice et al., 2023). Representative bedrock spectra were extracted from approximately co-located regions of interest (ROIs) in images from both left and right cameras, and collected into a database along with key image metadata (Rice et al., 2022b; Rice et al., 2023; St. Clair et al., 2022). We focus on in situ multispectral data taken by Mastcam-Z of dark rock surfaces that are relatively

dust-free and lack evidence for significant coverage by the purple coatings that are common throughout the crater floor (Garczynski et al., 2022). The work presented here complements and is informed by more detailed analyses of the Mastcam-Z multispectral data set on the Jezero crater floor (Rice et al., 2023).

2.2. SuperCam

SuperCam measures rock chemistry via Laser-Induced Breakdown Spectroscopy (LIBS), which uses a pulsed 1,064 nm laser beam to create a plasma from the target rock or soil, which is analyzed between 245 and 853 nm, with a field of view (FOV) of ~0.8 mrad. Geochemical analyses can be conducted with targets located from 1.5 to ~11 m, with a laser beam of ~170 μm diameter at 2.4 m and ~370 μm diameter at 5.5 m (Maurice et al., 2021; Wiens et al., 2021). Most observations include 30 shots, with the first five shots removed from analysis as they likely represent the dust layer (Maurice et al., 2021). We selected the best LIBS data (Udry et al., 2022) from natural rock surfaces, based on targets <6.5 m from the mast, lacking significant surface roughness (two consecutive autofocus fit curves performed during a raster are separated by less than 18 steps of the focus motor stage), and high intensities (>10^{14} photons/pulse/mm^2/sr/nm at the source). The points with low major-element oxide (eight elements; MOC) totals (<80 wt.%), were removed as they would indicate missing chemical species (e.g., OH, SO_4^{2-}, CO_3^{2-}), likely associated with secondary phases (Wiens et al., 2022). We averaged the LIBS data for each member (Artuby, Rochette, Roubion, Nataani, Chal, Content, Seitah) to retrieve approximate bulk chemistries. Detailed chemical data and analyses for the Maaz formation can be found in Udry et al. (2022) and Wiens et al. (2022), with complementary data from other geochemistry instruments presented in Simon et al. (2023).

SuperCam also acquires reflectance spectra of surfaces in the visible and short-wave infrared (VISIR) using a transmission spectrometer covering the 535–855 nm range in 6,000 channels and an acousto-optic tunable filter spectrometer covering the 1.3–2.6 μm range in 256 channels. The near-infrared wavelengths not detected by SuperCam (855–1300 nm) are partially covered by Mastcam-Z and fully covered by CRISM. The FOV of the instrument is 0.70 mrad in the visible range and 1.15 mrad in the short-wave infrared (Maurice et al., 2021), which corresponds to a few mm-wide analytical footprints for targets in the rover workspace. During the crater floor campaign, SuperCam measured more than 1500 VISIR spectra on rock targets and allowed the in situ detection of a wide range of minerals on the crater floor (e.g., olivine, pyroxene, oxyhydroxides, phyllosilicates, carbonates and sulfates; Mandon et al., 2023). Here, individual point spectra acquired on rock targets (both unabraded and abraded) were averaged for each specific member of the Maaz formation, excluding observations with saturation or major shadowing in the FOV.

2.3. RIMFAX

The RIMFAX GPR measures the shallow subsurface beneath the rover's path (Hamran et al., 2020). Radar reflections indicate changes in permittivity related to changes in density or composition, which often correlate with changes in lithology that can be used to infer subsurface structure. Here we used RIMFAX subsurface soundings to test our stratigraphic models developed based on surface outcrops imaged by Mastcam-Z.

The RIMFAX radar uses a gated Frequency Modulated Continuous Wave waveform over a range of 150–1,200 MHz. Soundings are collected every 10 cm along the rover traverse. At each location, three primary sounding modes are collected, each focusing on a different zone of the subsurface: Surface (surface reflection), Shallow (image from the surface down to ~7 meters), and Deep (from ~2 to tens of meters). All modes have the same depth resolution that will gradually change with depth from 10 cm close to the surface to 30 cm at 15 m depth. This partitioning is accomplished by varying the gating, time-delay, gain, and processing. As with any GPR, transmitted waves propagate downward until they are reflected back by shallow subsurface interfaces in geologic materials or structures, across which discontinuities in permittivity exist (e.g., Heggy et al., 2006; Jol & Bristow, 2003). The raw location of each sounding is given by surface attitude position and pointing software on the rover, which is fit between traverse end points localized by the Mars 2020 localization team. Radargrams used here display the absolute value of the complex signal value. Depth is estimated from time-delay with a constant subsurface velocity of 0.1 m/ns, consistent with typical permittivities measured from subsurface hyperbolas in RIMFAX data (Casademont et al., 2023).

2.4. Orbital Data Sets

Variations in surface texture across the crater floor were assessed using a mosaic of HiRISE (McEwen et al., 2007) high-resolution grayscale images (25–50 cm/pixel), with context from a Context camera (CTX; Malin et al., 2007) mosaic. Both mosaics were produced by the USGS (Fergason et al., 2020). Regional context was assessed using elevation data from Mars Orbiter Laser Altimeter (MOLA; Zuber et al., 1992) and High-Resolution Stereo Camera (HRSC; Jaumann et al., 2007), blended to create a global digital elevation model (DEM). The DEM was used to colorize a global daytime infrared mosaic from Thermal Imaging System (THEMIS; Christensen et al., 2004). Both datsets are available in the Java Mission-planning and Analysis for Remote Sensing software package (JMARS; Christensen et al., 2009).

Mineralogical variations were assessed using reflectance spectra from the CRISM (Murchie et al., 2007) hyperspectral imaging spectrometer, which acquires high spatial resolution reflectance spectra across the visible, near-infrared, and short-wave infrared wavelength regions (VNIR/SWIR, 350–2,600 nm, ∼18–36 m/pixel). CRISM mapped targeted reduced data records (MTRDR) on the NASA Planetary Data System (PDS) have undergone processing to suppress atmospheric and instrumental effects to produce "corrected" I/F spectra (Seelos et al., 2016). MTRDRs include a suite of spectral parameters, derived from the I/F cubes and refined to reduce noise (Viviano-Beck et al., 2014). RGB color composites were generated in Horgan et al. (2020a) from these spectral parameters to evaluate spectral diversity across the crater floor. CRISM spectral parameters from Viviano-Beck et al. (2014) used here include HCPINDEX2 and LCPINDEX2, which highlight spectral shapes similar to the 1 and 2 μm Fe bands in high-Ca pyroxene (HCP; e.g., augite and diopside) and low-Ca pyroxene (LCP; e.g., enstatite, ferrosilite, and some pigeonites), and BD1300, which highlights absorption at 1.3 μm that is strongest in olivine but also weakly present in Fe-bearing glass and Fe-bearing plagioclase feldspar. These parameters were combined into an RGB color composite as shown in Figure 1b. Spectral interpretations from these maps were verified using detailed spectral analysis and comparison to laboratory endmembers. I/F spectra were extracted from each individual MTRDR and ratioed with the average spectrum from all spectrally neutral pixels in that cube to bring out subtle spectral features. Spectrally neutral terrains were determined using standard CRISM spectral parameters, as described in Horgan et al. (2020a).

3. Morphology

3.1. Orbital Context

From orbit, the upper surface of the crater floor is defined by distinctive lobate margins in most locations, and most commonly, a rough, fractured, and cratered appearance with variable regolith cover (Figure 1c). This unit, previously mapped as the "Crater floor - fractured rough" (Cf-fr) unit of Stack et al. (2020), appears to overlie and embay a ridged and layered unit mapped as "Crater floor - fractured 1" (Cf-f-1). The region of Cf-fr explored by Perseverance has been named the Maaz formation. Perseverance remote sensing and radar observations confirm that Cf-fr/Maaz overlies Cf-f-1 (Farley et al., 2022), which has been named the Seitah formation in the region of the traverse, and is interpreted as an eroded olivine cumulate originating in a lava lake or thick lava flow (Liu et al., 2022). Based on the lobate margins, rough texture, and embaying relationships with Cf-f-1, previous studies hypothesized that Cf-fr could be a lava flow, but a pyroclastic or sedimentary origin could not be ruled out based on orbital data alone (Goudge et al., 2015; Horgan et al., 2020a; Schon et al., 2012; Sun & Stack, 2020).

A more detailed analysis of surface textures in HiRISE images near the traverse and delta reveals that the surface texture of Cf-fr/Maaz formation is quite variable, and generally falls into four morphotypes: (a) Rough hummocks dominated by large and rounded boulders and often exhibiting impact craters (Figure 2b), (b) Smooth regolith-poor terrains fractured into meter-scale polygons (Figure 3a), (c) Flat fragmented blocks embedded in smooth and dark terrains (Figure 4b), and (d) Smooth and dark terrains with large linear or radial fractures. Rough terrains dominate most of the crater floor east of the Mars 2020 landing site, but smooth terrains dominate west and north of the landing site and close to the delta (Figure 1c).

3.2. In Situ Observations

On the ground, Mastcam-Z images looking east of the landing site show that the rough hummocks are indeed composed of massive boulders (tens of cm to meters in size) and some in place massive outcrops forming local

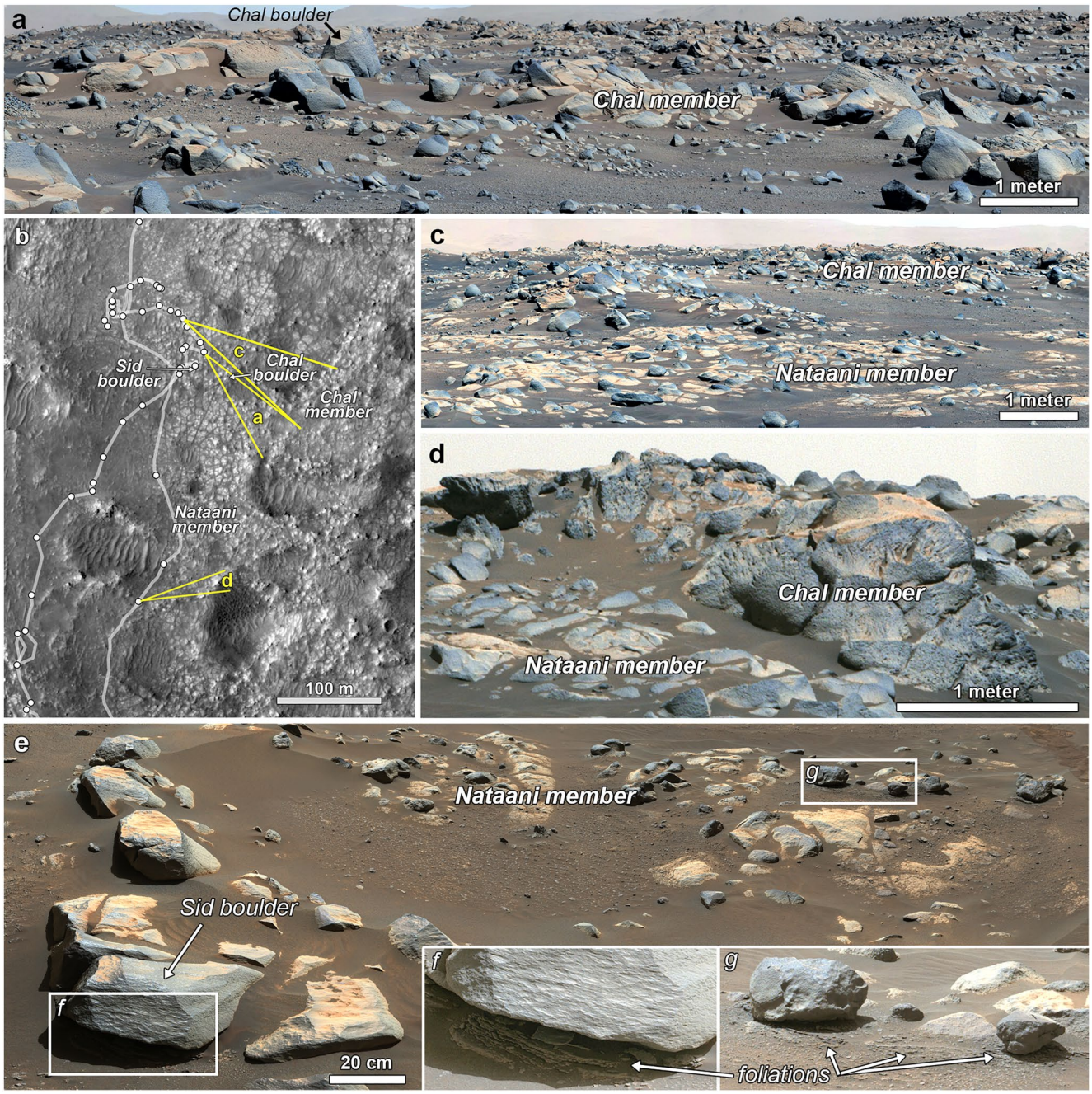

Figure 2. Chal and Nataani outcrop morphologies near the Octavia E. Butler landing site. (a) Boulders and hummocks of the Chal member from Mastcam-Z (sol 78 zcam08041) and (b) in the HiRISE mosaic (Figure 1c). (c) Massive vesicular Chal outcrops at the edge of the roughest zones (sol 357 zcam08388). (d) Nataani polygonal surfaces transitioning to Chal boulders (sol 64 zcam08109). (e) Sid block of the Chal member, where the Hahonih and Atsah samples were acquired (sol 364 zcam08396), overlying Nataani benches and (f) foliations that are visible in a contrast enhanced image (sol 53 zcam08100).

topographic highs (Figure 2a). This terrain is demarcated as the Chal member of the Maaz formation ("Ch'ał" in Navajo). The largest outcrops and boulders were not encountered at close range, but some smaller boulders along the traverse show possible vesicular textures. No clear layering of any variety was observed within the Chal member. Perseverance abraded (Alfalfa abrasion) and collected a paired sample (Hahonih and Atsah) from a large block known as Sid that was inferred to be part of the Chal member (Figure 2e).

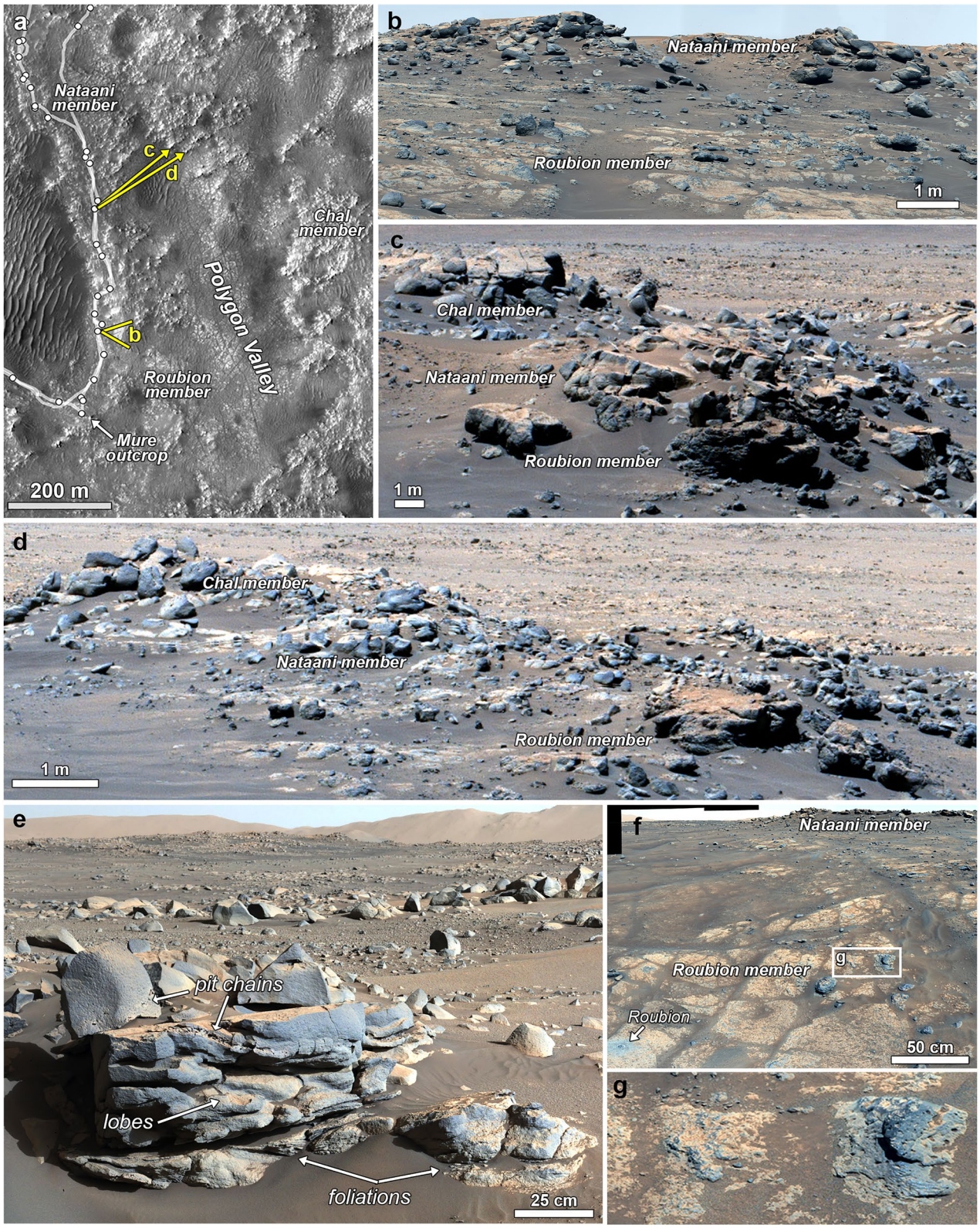

Figure 3. Outcrops around Polygon Valley, south of the landing site. (a) Context view from the HiRISE mosaic (Figure 1c). (b) Entrance to Polygon Valley, showing rough, dark, and pitted Roubion polygons with subtle layering transitioning to a massive layered capping outcrop, interpreted as Nataani (sol 138 zcam08147). (c, d) To the northeast, showing outcrop views of the dark, rough, and pitted Roubion layers overlain by massive layers and boulders, interpreted as Nataani and Chal, respectively (Sol 132 zcam08134). (e) To the south at Mure, a possible outcrop of Nataani member (sol 168 zcam08180), (f, g) which is underlain by dark pitted Roubion member pavers (sol 163 zcam08172).

Near the landing site, Chal member boulders overlie smooth to knobby meter-scale polygonal surfaces that sometimes appear to form local benches, demarcated as the Nataani member ("Naat'áanii" in Navajo; Figures 2c–2e). Some Nataani blocks exhibit sinuous chains of cm-scale pits that may be possible vesicle trains. The Sid block is inferred to preserve the contact between Chal and Nataani, as thin foliations are observed beneath Sid and similar blocks throughout the area (Figures 2f and 2g). Similar foliations are observed in cross-section at the Mure outcrop ~1 km south of the landing site (Figure 3e), where they more strongly resemble flow banding in igneous rocks (Alwmark et al., 2023). Mure also exhibits pit chains and smooth surfaces at the top of the outcrop that are similar to Nataani, as well as lobate morphologies in outcrop that are consistent with pāhoehoe lavas (Figure 3e, Alwmark et al., 2023). No samples or abrasions were conducted on rocks of the Nataani member.

The Mure outcrop forms the southern margin of a 200–300 m wide and 5–10 m deep valley that cuts into the Maaz formation, colloquially known as "Polygon Valley" (Figure 3a), because it is floored by flat-lying, meter-scale polygonal surfaces of the Roubion member (Figures 3b and 3f), which was abraded by Perseverance (Guillaumes abrasion). This member was not observed in cross section near the rover, but exposed blocks within the member are distinctive, exhibiting a dark tone and pitted and rough texture with subtle layering (Figure 3g). This texture is similar to exposures of dark, pitted, and rough-textured layers exposed in the deepest parts of Polygon Valley to the NE, 200 m from the traverse, suggesting that these may be outcrops of the Roubion member (Figures 3c and 3d). In this northern part of the valley, the outcrops transition to polygonal surfaces also consistent with Roubion, which together cover an elevation range of up to 8 m, potentially representing one of the thickest outcrops of an individual member of the Maaz formation observed by Perseverance.

The outcrop expression of the Maaz formation changes substantially to the west of Mure at Artuby ridge, along the southern contact with the Seitah formation. Artuby is defined by apparent layers ranging from a few to tens of cm in thickness that dip to the southeast, with variable layer morphology (Alwmark et al., 2023). The sharp ridge top and thus the margin of the Maaz formation at this location is typically characterized by resistant and cliff-forming blocks of the Rochette member (Figure 4e), which in outcrop exhibit linear fabrics resembling planar fractures or joints rather than layers (Figure 4a). Below the resistant Rochette member cap, the Artuby ridge outcrop transitions to knob-forming and rounded or even recessive and friable layers of the Artuby member (Figures 4d and 4g). The surface expression of the plains to the south of Artuby ridge is characterized by exposure of more resistant Rochette layers as fractured blocks, embedded in dark regolith that may be sourced from Rochette or the more friable Artuby layers (Figure 4f). The Rochette member was abraded (Bellegarde abrasion) and sampled (Mondenier and Montagnac samples) in one of these fragmented surface blocks named Rochette (Figure 4f), and the Artuby member was abraded at the Rimplas outcrop (Montpezat abrasion, Figure 4g).

3.3. Synthesis of Orbital and In Situ Data

The rough hummocks observed from orbit in the Maaz formation appear to correspond to the Chal member, the smooth polygonal surfaces appear to correspond to the Nataani and Roubion members, and the fragmented blocks embedded in smooth terrains appear to correspond to the Rochette and Artuby members. The contrast between the surface expressions of the Nataani and Chal members and the Rochette and Artuby members is most apparent to the south of the rover traverse, where the rough landscape south of Mure of Nataani and Chal member boulders and hummocks (Figure 1c) sharply transitions south of Artuby ridge (Figure 4b) to the smooth landscape of fractured blocks and regolith of the Rochette and Artuby members (Figure 4f).

4. Spectral and Chemical Properties

4.1. CRISM

VNIR/SWIR spectral signatures offer one of the clearest distinctions between the Seitah and Maaz formations from orbit, as highlighted in the CRISM mafic RGB combination in Figure 1, where Seitah shows up as red and Maaz as blue to green. Ratioed CRISM spectra in Seitah exhibit a deep and broad band centered between 1.07 and 1.3 μm, with a strong shoulder between 1.3 and 1.5 μm that is attributed to olivine (red spectra in Figure 5). These areas exhibit high BD1300 values, which causes them to show up as bright red in the CRISM mafic RGB combination in Figure 1. Some variability is observed in the shape and position of the band, which could be related to compositional variations in the olivine, but as these variations often correlate with sediment cover, they are instead likely related to variations in grain size in outcrop versus regolith as well mixing with more diverse regolith materials (Horgan et al., 2020a). Perseverance observations confirm that Seitah bedrock is composed of mm-size olivine

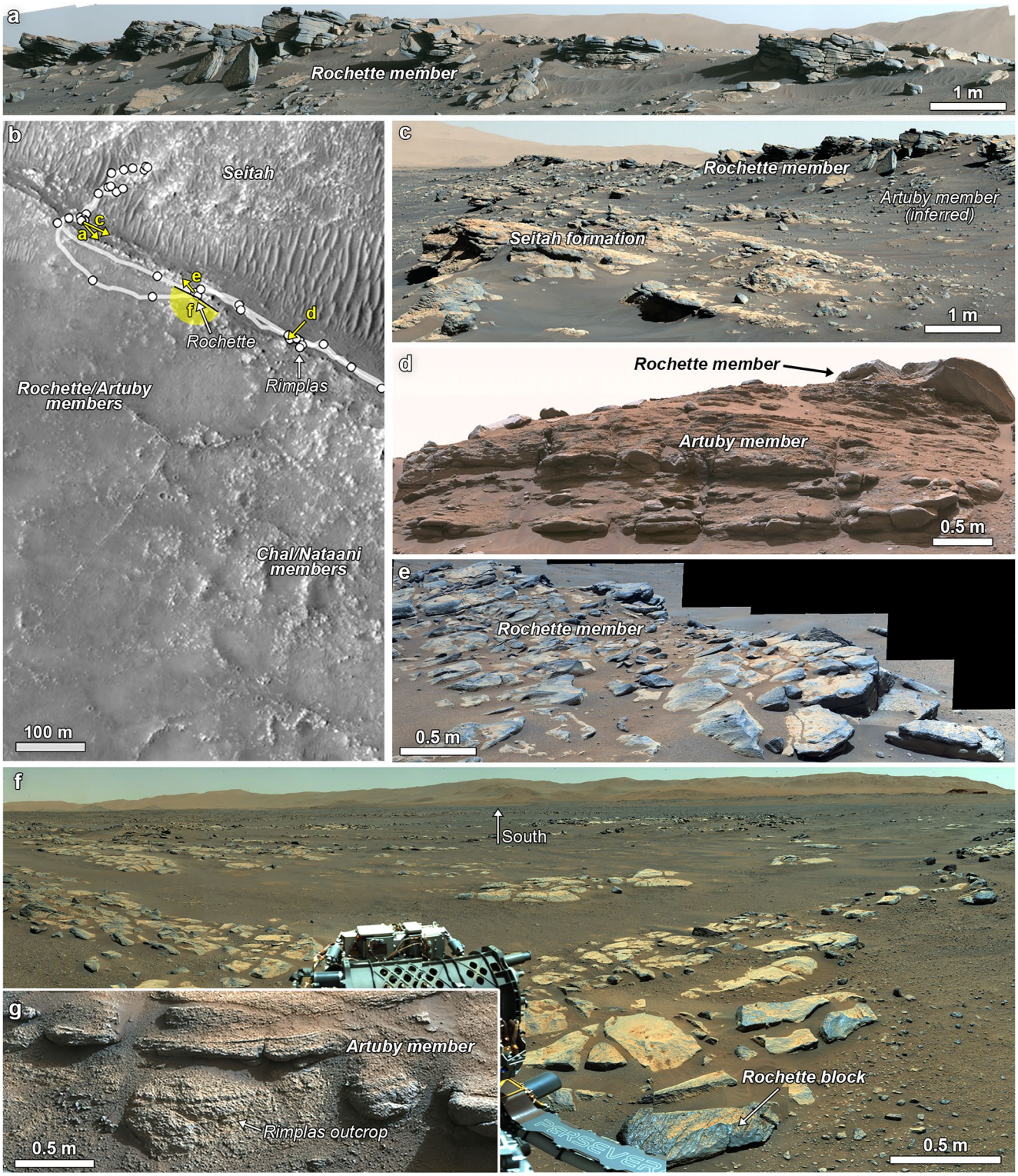

Figure 4. Outcrops along Artuby ridge. (a) Rochette member resistant cap showing planar jointing (sol 289 zcam08314). (b) Context view from the HiRISE mosaic (Figure 1c) over Artuby ridge area showing image locations. (c) Tilted beds of the Seitah formation underlying Rochette and Artuby members (sol 305 zcam03281). (d) Thin recessive and thicker knobby resistant layers in the Artuby member (sol 342 zcam03309). (e) Overlooking Rochette member on ridge top (sol 180 zcam08194). (f) Landscape view looking south of Artuby ridge from Mastcam-Z (sol 181 zcam08199). (g) Outcrop view of Rimplas abrasion target in Artuby member (sol 343 zcam07101).

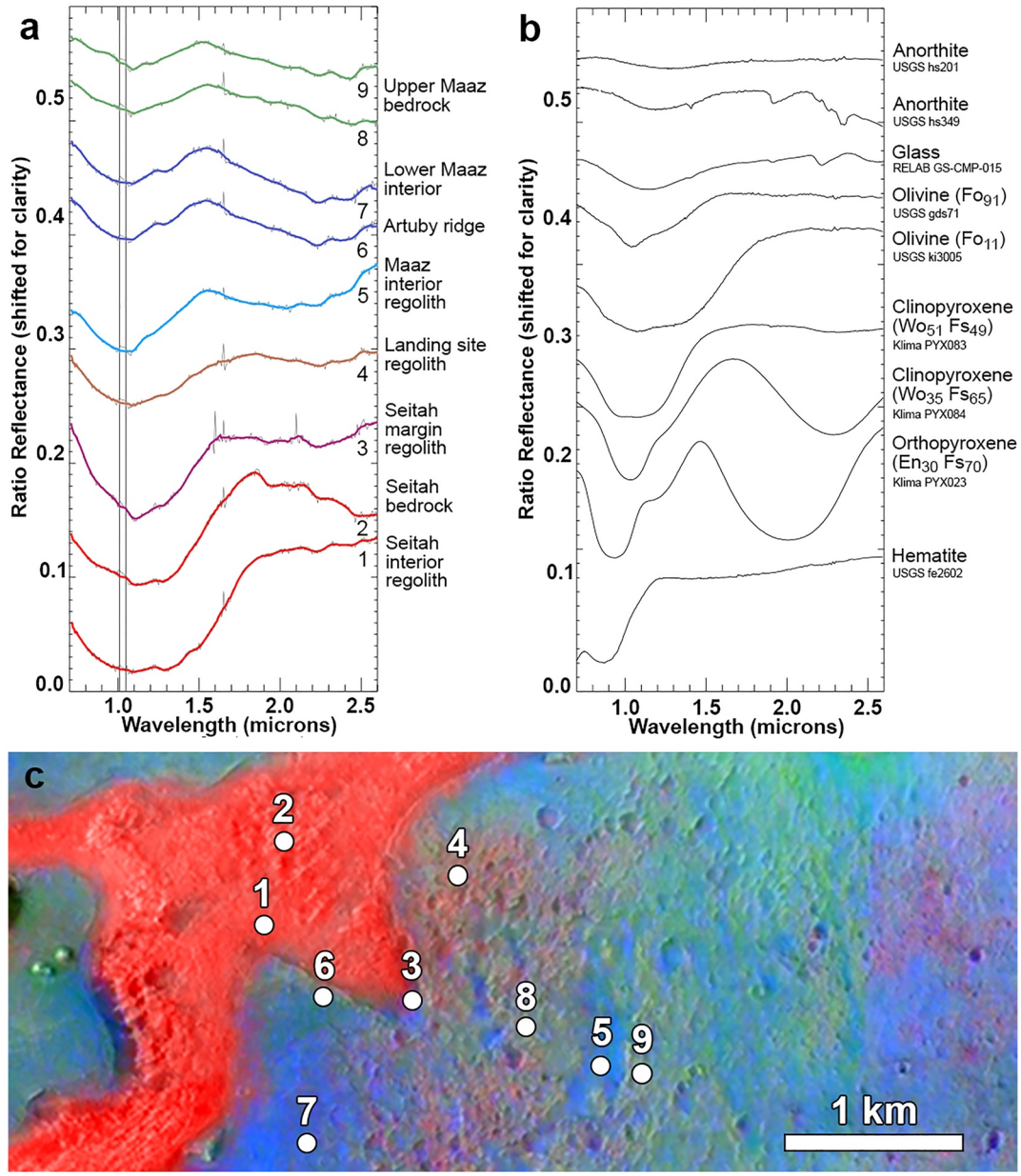

Figure 5. Orbital spectral properties of the Maaz and Seitah formations. (a) Compact Reconnaissance Imaging Spectrometer for Mars (CRISM) ratio spectra of the western crater floor, source image HRL000040FF. See Figure S1 in Supporting Information S1 for corresponding I/F spectra. Vertical lines indicate the position of the join between the S- and L-detectors. Thin gray lines are raw spectra, thick colored lines are smoothed. Colors and numbers indicate color and location in panel (c). (b) Laboratory spectra of mafic minerals (USGS: Kokaly et al., 2017; Klima: Klima et al., 2011; RELAB: Milliken, 2020). Note that the second anorthite spectrum shows secondary alteration bands between 1.4 and 2.3 μm. (c) CRISM red, green, and blue combination over HiRISE (Figure 1d). See Figure S1 in Supporting Information S1 for regions of interest coordinates.

grains in a clinopyroxene (CPX) -dominated matrix (Beyssac et al., 2023; Liu et al., 2022; Wiens et al., 2022), and that surface regolith is a mix of coarse olivine grains and finer pyroxene-dominated grains (Vaughan et al., 2023).

CRISM spectral signatures show a strong correlation with surface morphology in the Maaz formation. Smooth surfaces south of Artuby ridge attributed to the Rochette and Artuby members exhibit a weaker and more symmetric band centered closer to 1 μm, without the strong olivine shoulder (spectra 7–8 in Figure 5a). This band is

paired with a broad and shallow band centered near 2.2 μm, which is consistent with HCP. The specific positions of the bands (most commonly 1.00–1.04 and 2.15–2.20 μm) are most consistent with Fe-rich and moderately calcic CPX (e.g., $Wo_{35}Fs_{65}$ augite in Figure 5b, Cloutis & Gaffey, 1991a; Klima et al., 2011), and the shift of the interband peak to near 1.5 μm is consistent with mixing with low abundances (∼10%–30%) of orthopyroxene (OPX, Horgan et al., 2014). Absorption in these spectra between 2.12 and 2.46 μm relative to 1.6 and 2.53 μm causes high values of HCPINDEX2, which causes these areas to show up as blue in the CRISM mafic RGB combination in Figure 1. However, at CRISM resolution (18–36 m/pixel) it is unclear if these signatures are related to bedrock, surficial regolith, or both.

Rough surfaces, including those attributed to the Chal and Nataani members above, lack a 2 μm band that would suggest the presence of most common pyroxenes (Cloutis & Gaffey, 1991a). Instead, these areas only exhibit a broad and weak band near 1 μm, with center positions varying from 1.08 to 1.20 μm (spectra 8–9 in Figure 5a). These areas also often exhibit a weak band at 0.86 μm superposed on this broader band, consistent with crystalline hematite. The broad band could be due to olivine, and in some locations can be attributed to olivine in surface regolith. For example, the Perseverance landing site near the margin of Seitah is covered by dark regolith and shows bands consistent with an olivine/pyroxene mixture (spectrum 4 in Figure 5a). However, elsewhere in the Maaz formation the broad band is associated with rough and high-thermal inertia bedrock outcrops. In addition, away from the Seitah margin, regolith becomes dominated by strong HCP bands, including a strong broad band at 2 μm that is not present in the Maaz bedrock (spectrum 5 in Figure 5a).

The fact that the 1.08–1.2 μm band in Maaz bedrock is relatively weak suggests that a different mineral with a broad band >1.05 μm may be contributing, such as Fe-bearing feldspar, Fe-bearing glass, HCP, or a mixture of these minerals (Figure 5b, Adams & Goullaud, 1978; Cloutis & Gaffey, 1991a, 1991b; Horgan et al., 2014; Klima et al., 2011). The presence of this weaker band causes some rough areas near the landing site to exhibit muted red colors (BD1300) in the CRISM mafic RGB combination map in Figure 1. Other areas show as green due to the strong downturn beyond 1.5 μm that is also common in these spectra, resulting in elevated LCPINDEX2 values.

4.2. Mastcam-Z

4.2.1. Natural Surfaces

Outcrops of the Maaz formation show spectral variations in Mastcam-Z images that correlate well with morphologic facies described above (see also Bell et al., 2022; Rice et al., 2023). In particular, we find a sharp spectral division for dark rock surfaces between Maaz formation members: Chal, Nataani, and Roubion member rocks typically exhibit strong red slopes between 445 and 750 nm and a sharp peak near 750 nm, while Rochette and Artuby member rocks typically exhibit relatively flat spectra 600–1,000 nm with peaks often shifted to below 700 nm (Figure 6a). Stronger absorptions at short wavelengths in Chal, Nataani, and Roubion are likely due to ferric iron in primary or secondary minerals, suggesting more oxidizing conditions during emplacement or later alteration compared to Rochette and Artuby.

Maaz formation rocks also show a variety of broad absorption bands at longer wavelengths consistent with Fe-bearing minerals (Figure 6). Three types of absorption bands are the most common. (a) A narrow to broad V-shaped band centered near 860 nm, consistent with crystalline red hematite (Horgan et al., 2020b; Morris et al., 1985) and most common in Chal and Roubion. (b) A broad band centered between 900 and 950 nm, consistent with OPX or Ca-poor and Fe-rich CPX (e.g., ferrosilite or pigeonite, Cloutis & Gaffey, 1991a), or possibly some ferric minerals like nontronite or goethite (Haber et al., 2022; Rudolph et al., 2022; Townsend, 1987). This band is variably present in all members. (c) A broad band superposed on a blue slope toward the end of the wavelength range, potentially suggesting a very broad band with a center >1,030 nm like in olivine, CPX, Fe-bearing glass, or feldspar (Horgan et al., 2014). Nataani exhibits the broadest and deepest >1,000 nm absorption bands, with some occurrences in Roubion as well. In many cases, these absorption bands may combine to create a more complex shape (e.g., both hematite and pyroxene bands in Roubion, Figure 6a).

Spectral parameters applied to Mastcam-Z images of Maaz formation targets in Figure 7 clearly demonstrate the spectral differences between the Maaz members. These images are color combinations of spectral parameters measuring slopes (via reflectance ratios) and band depths. In this Mastcam-Z "mafic" RGB parameter combination, red is the ratio R0R/R1 (630/800 nm), which is high for spectra with peaks shifted to short wavelengths, and here indicates relatively unoxidized surfaces dominated by ferrous silicates like olivine and HCP. Green

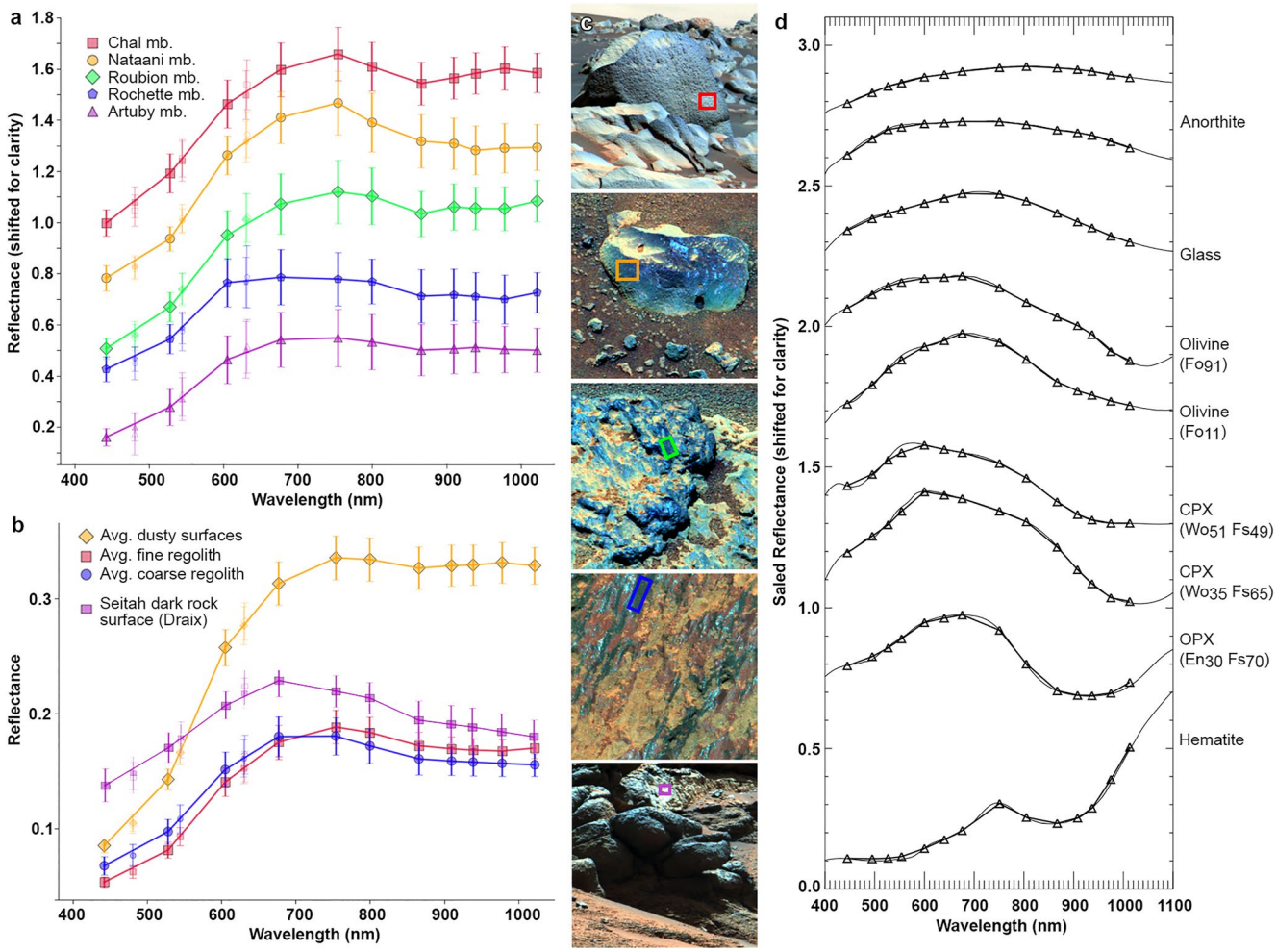

Figure 6. Summary of Mastcam-Z multispectral data from the crater floor. (a) Representative spectra of Maaz formation members from dark, relatively uncoated surfaces, scaled at 600 nm and stacked for clarity. (b) Average spectra from fine- and coarse-grained regolith targets in the Maaz and Seitah formations, average dusty surfaces (Vaughan et al., 2023), and typical Seitah dark surfaces (Rice et al., 2023). (c) Source images, top to bottom: Chal boulder, sol 372 zcam03330; Tseebii cobble, sol 112 zcam03161; Mont Brune outcrop, sol 145 zcam03186; Rochette block, sol 187 zcam03213; and Artuby outcrop, sol 175 zcam03310. (d) Lab spectra in Figure 5 convolved with Mastcam-Z filter bandpasses.

is BD910, defined as the band depth at R3 (910 nm) relative to R1 (800 nm) and R5 (978 nm), which is high for spectra with strong ~900 nm bands, including LCP and ferric alteration minerals. Blue is the ratio R1/R5 (800/978 nm), which is high for spectra with absorption bands centered at longer wavelengths like olivine, HCP, Fe-bearing glass, or feldspar. In this color combination, the Chal member rock Sid is dominated by green (Figure 7a) and Roubion is green and magenta (Figure 7b), while the Rochette member rock Rochette is red and magenta (Figure 7c) and the Artuby member rock Rimplas is blue and magenta (Figure 7d).

4.2.2. Abrasion Patches

We can investigate the petrologic origin of these natural surface spectral properties by using the abrasion patches created by Perseverance on four Maaz rocks from different members (Figure 7). These patches are created by percussive grinding of an area ~5 cm across to a depth of 4–8 mm (Moeller et al., 2021). This process removes surficial coatings and textures but not deeper weathering rinds. While most Maaz rocks show uniform surface color, all abrasion surfaces showed significant color variation at the sub-mm-scale that are resolvable by Mastcam-Z (Figure 8; 0.15–0.2 mm/pixel for the abrasion patches, making features ~0.5 mm resolvable). In higher resolution images from Wide Angle Topographic Sensor for Operations and eNgineering (WATSON; Minitti et al., 2021) and SuperCam Remote Micro Imager (RMI; Maurice et al., 2021) as shown in Figure 8, these color variations often correspond to coarse and angular primary grains, supporting an igneous interpretation

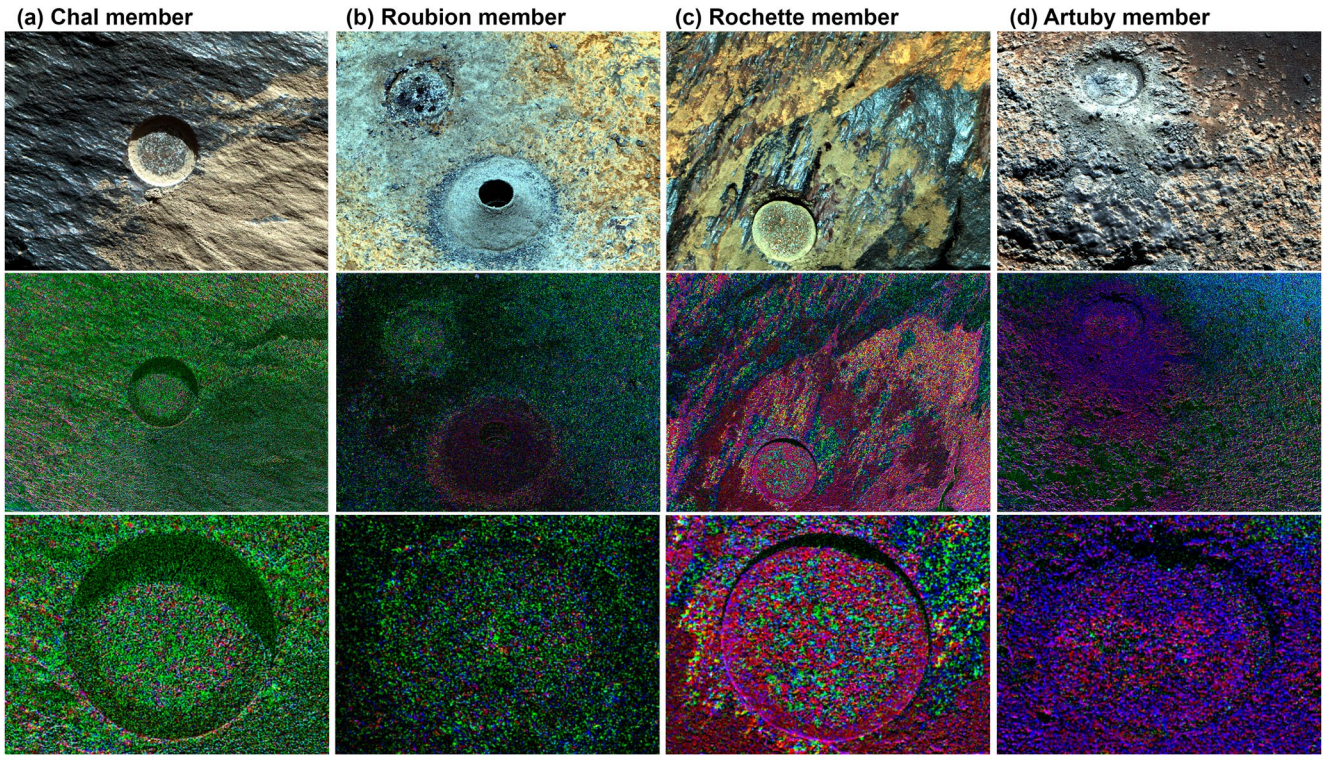

Figure 7. Mastcam-Z images of Maaz formation abrasion patches, where abrasion patches are ~5 cm in diameter. (a) Alfalfa abrasion on the Sid block near the boundary of the Chal member (sol 368 zcam03328). (b) Guillaumes abrasion on the Roubion paver in the Roubion member (sol 166 zcam3200) (c) Bellegarde abrasion on the Rochette block in the Rochette member (sol 187 zcam03213). (d) Montpezat abrasion on the Rimplas outcrop in the Artuby member (sol 350 zcam03318). (top row) Enhanced color view from right Bayer images, (middle row) "mafic" red/green/blue spectral parameter combination as described in Section 4.2 for the full scene and (bottom row) within the abrasion patches. All images are stretched as red (R0R/R1): 0.95–1.15, green (BD910): 0.02–0.1, and blue (R1/R5): 1.04–1.15.

for the Maaz formation that is also inferred from outcrop texture and mineralogy (Alwmark et al., 2023; Farley et al., 2022; Simon et al., 2023; Udry et al., 2022; Wiens et al., 2022).

Throughout the Maaz formation abrasion patches, hematite signatures are associated with visible red staining while pyroxene signatures are associated with gray grains, but the two signatures are often intimately mixed at the pixel scale of Mastcam-Z to produce complex absorption bands with intermediate properties. The Alfalfa abrasion patch in the Chal member exhibits red areas with strong hematite signatures and gray areas with weak broad pyroxene bands (Figure 8a), and the mixture of these two minerals appears to produce very broad bands with centers near 860 nm on the natural surfaces and tailings.

Alfalfa also exhibits large white feldspar crystal laths that exhibit minimal absorption <600 nm suggesting little ferric iron, and either flat slopes >600 nm consistent with typical (Fe-poor) feldspars or blue slopes suggesting the presence of ferrous iron, most likely due to sub-pixel mixing with pyroxene and/or Fe^{2+} substitution in anorthite (blue and cyan spectra, Figure 8a, Adams & Goullaud, 1978). Similar spectra are present in Bellegarde and Montpezat, associated with light gray areas (blue spectra, Figures 8c and 8d).

Hematite signatures are strongest in Chal but appear to weaken downsection in the Maaz formation. The Bellegarde abrasion patch in the Rochette member shows a clear mixing trend between moderate hematite signatures and pyroxene, in which red areas with weak hematite bands gradually shift their centers to closer to 900 and then >900 nm as the density of black to gray grains increases (Figure 8c). These weak pyroxene signatures also appear to dominate the natural surface and tailings spectra, which are notably not oxidized compared to the Alfalfa abrasion patch nearby natural surfaces in the Chal member. Hematite bands are nearly absent in the Montpezat abrasion patch in the Artuby member, which shows no strong pyroxene signatures but does show some spectra with blue slopes to long wavelengths that could suggest bands centered >1,000 nm from other mafic minerals (green and cyan spectra, Figure 8d).

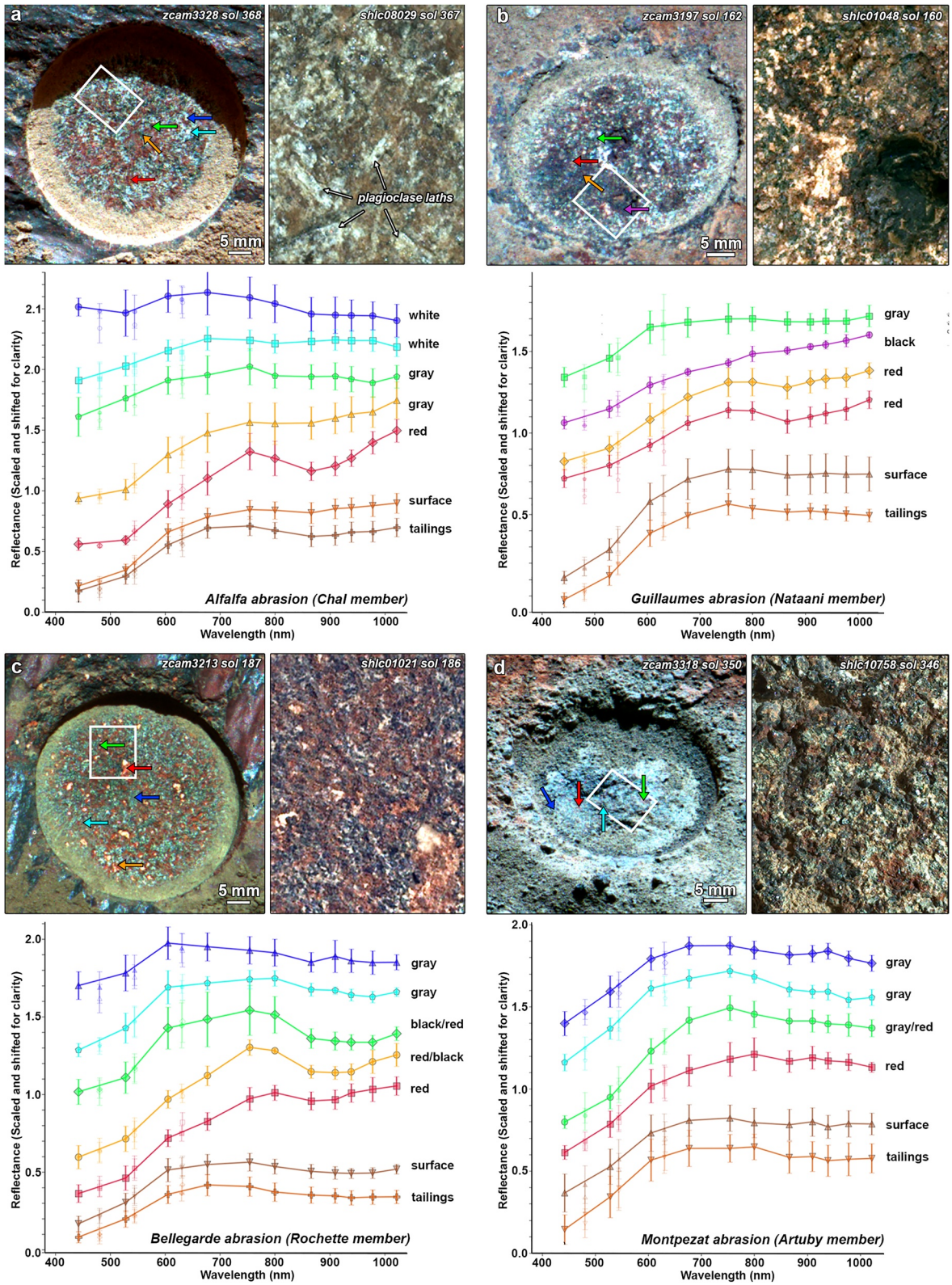

Figure 8. Mastcam-Z spectra of Maaz formation abrasion patches compared to natural surfaces and borehole tailings, with L256 enhanced color image showing locations of spectra, where arrow colors correspond to spectra colors. White box indicates location of Wide Angle Topographic Sensor for Operations and eNgineering image at right showing igneous textures in the abrasion patches. (a) Alfalfa abrasion on the Sid boulder in the Chal member, (b) Guillaumes abrasion on the Roubion paver in the Roubion member, (c) Bellegarde abrasion on the Rochette block in the Rochette member, and (d) Montpezat abrasion on the Rimplas outcrop in the Artuby member.

The Guillaumes abrasion patch on Roubion shows evidence for alteration in addition to oxidation. Guillaumes exhibits moderate hematite signatures in dark brown to red regions that are consistent with the overall trend downsection (orange and red spectra, Figure 8b), but these are mixed with black areas that exhibit very strong red spectral slopes and no discernible absorption bands (purple spectrum, Figure 8b). These strong red slopes could be consistent with opaque minerals like Mn-oxides and sulfides, or with some mixed-valence Fe-bearing phyllosilicates like greenalite. The black areas are found throughout the abrasion patch but are concentrated within and near surficial pits, suggesting a weathering rind.

A weathering rind at Roubion is further supported by the spectral differences between the abrasion tailings and borehole tailings produced during the attempted coring of he Roubion member sample. In Figure 7b, the abrasion patch is largely green in the Mastcam-Z "mafic" parameter combination, and the abrasion tailings are black, suggesting low spectral contrast. However, the borehole tailings are magenta, consistent with much stronger spectral slopes. Dark surfaces on boulders in the area that are inferred to be Roubion based on morphology also show a magenta color in this parameter combination. This suggests that the coring process, which typically extracts material from up to 6–8 cm deep (Moeller et al., 2021), penetrated well through the weathering rind.

4.3. SuperCam

4.3.1. VISIR

SuperCam VISIR spectra are highly complementary to Mastcam-Z multispectral data. While Mastcam-Z provides wide coverage, outcrop-scale context for VNIR multispectral signatures, and direct connection of spectral signatures to specific grains in the abrasion patches, SuperCam VISIR expands our wavelength range out to longer wavelengths, 1,300–2,500 nm. This range can detect the far side of wide 1,000 nm mafic mineral absorptions due to minerals like olivine, the ∼2,000 nm iron band in most pyroxenes, and narrow absorptions between 1900 and 2,500 nm due to alteration minerals.

Figure 9 shows average SuperCam VISIR spectra for Maaz formation members (Mandon et al., 2023). The members display overall similar spectral shapes, dominated by a broad band between 700 and 1,700 nm consistent with olivine, feldspar mixtures, HCP, and some mixed valence Fe-bearing phyllosilicates. This band is strongest in the Chal, Nataani, and Roubion members and weakest in the Rochette and Artuby members, consistent with the strength of the short wavelength side of this band in Mastcam-Z spectra of these members (Figure 6a). None of the average spectra show clear 2,000 nm pyroxene bands, but independent components analysis (ICA) of the abrasion patches indicates the presence of a strong broad band near 2,300 nm consistent with HCP (Mandon et al., 2023). The average spectra also exhibit strong bands due to hydration at 1,400 and 1,900 nm, as well as weak variable bands between 2,200 and 2,500 nm due to alteration minerals such as phyllosilicates and sulfates (Mandon et al., 2023).

4.3.2. SuperCam LIBS

Elemental chemistry from SuperCam LIBS of natural surfaces shows that the Chal and Nataani members are chemically distinct from the Rochette and Artuby members (Figure 10, Udry et al., 2022; Wiens et al., 2022). Chal and Nataani member averages are similar, and show higher SiO_2 than Rochette/Artuby (∼52 vs. ∼46 wt.%). Roubion falls in the middle of the two groups for SiO_2 (∼49 wt.%). The Maaz members also show similar abundances for other cations, except that the Artuby member shows higher MgO, CaO, and TiO_2 and slightly lower alkalis than the rest of Maaz. These calculations support early results from SuperCam that suggested that the Maaz formation shows an overall increase in both silica and alkalis upsection (Wiens et al., 2022). The Content member, which is a texturally distinct and olivine-poor unit found within the Seitah formation, is most similar to Chal in these plots (although slightly more enriched in Al_2O_3, 12 wt.%), potentially supporting a similar igneous origin (Brown et al., 2023; Udry et al., 2022; Wiens et al., 2022).

In some cases, LIBS measurements exhibit compositions consistent with a single mineral, and thus can be used to assess the coarser-grained (>∼300–500 μm) component of the rocks. Udry et al. (2022) detected 20 pyroxene grains in the Maaz formation using this method, where the pyroxenes form a trend from augite ($Wo_{30–50}En_{10–22}Fs_{29–55}$) to a ferrosilite-like Fe-rich low-Ca pyroxene ($Wo_{3–9}En_{4–18}Fs_{73–93}$). No other primary minerals were detected, suggesting that high- and low-Ca clinopyroxene (CPX, augite and pigeonite) dominate the coarsest grains.

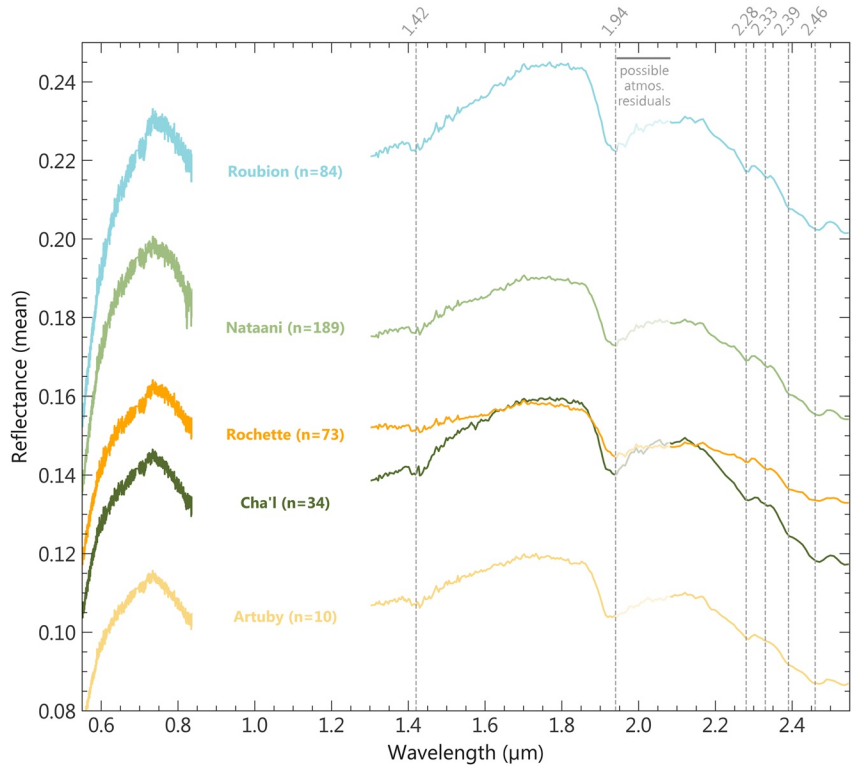

Figure 9. Average SuperCam visible and short-wave infrared (VISIR) spectra from Maaz members (Mandon et al., 2023), including both dusty and Laser-Induced Breakdown Spectroscopy-cleared natural surfaces and abrasion patches (n: number of individual point spectra averaged). Vertical lines indicate the position of narrow absorption bands associated with alteration minerals.

Mineral assemblages derived from Cross, Iddings, Pirsson and Washington (CIPW) normative modal abundances show that feldspar should be abundant in Maaz formation rocks, where equal proportions (~40% each) of pyroxene and feldspar were modeled in the Chal and Nataani members (averaged together). Twice as much pyroxene as feldspar (~60% vs. ~30%, respectively) was modeled in the Roubion, Rochette, and Artuby members (averaged together), with the remainder corresponding to quartz and minor phases, and no olivine modeled in either group (Udry et al., 2022).

4.4. Origin of Maaz Formation Spectral Signatures

Based on in situ chemistry and spectral data, the mineralogy of the Maaz formation is dominated by a mixture of feldspar with Ca-poor and Ca-rich clinopyroxenes, both relatively or very enriched in iron, with small quantities of hematite, phyllosilicates, sulfates, and other accessory minerals. Pyroxene would be expected to dominate reflectance spectra of the Maaz formation between 900 and 2,500 nm. The Ca-poor pyroxene endmember identified by LIBS would be expected to exhibit absorption bands near 940 and 2,100 nm (e.g., Wo_{35} CPX in Figure 5b, Klima et al., 2011), and the former is consistent with bands in Mastcam-Z spectra in the Maaz formation and the main spectral signature of the fine regolith. The Ca-rich pyroxene endmember (augite) typically exhibits absorption bands near 1,020 and 2,300 nm, where the latter band position is consistent with ICA of SuperCam abrasion patch spectra in the Maaz formation (Mandon et al., 2023) and both band positions are similar to CRISM ratio spectra of regolith-dominated terrains south of Artuby ridge.

However, CRISM and SuperCam VISIR spectra of Maaz formation bedrock are not consistent with pyroxene, and are instead dominated by a single broad band between 0.7 and 1.5 μm, centered between 1.1 and 1.2 μm, and the short wavelength side of this band is commonly observed in Nataani rocks by Mastcam-Z. SuperCam LIBS data clearly shows that this broad band is not due to olivine, as significant olivine is not directly detected or inferred in the Maaz formation. Glass is also not expected to be a significant component of the coarsely crystalline lavas in the Maaz formation. It is common for pyroxene-dominated lavas to exhibit only the 1,000 nm pyroxene band, as the weaker 2,000 nm band can be obscured by opaque oxide minerals or other optical effects that lower overall spectral

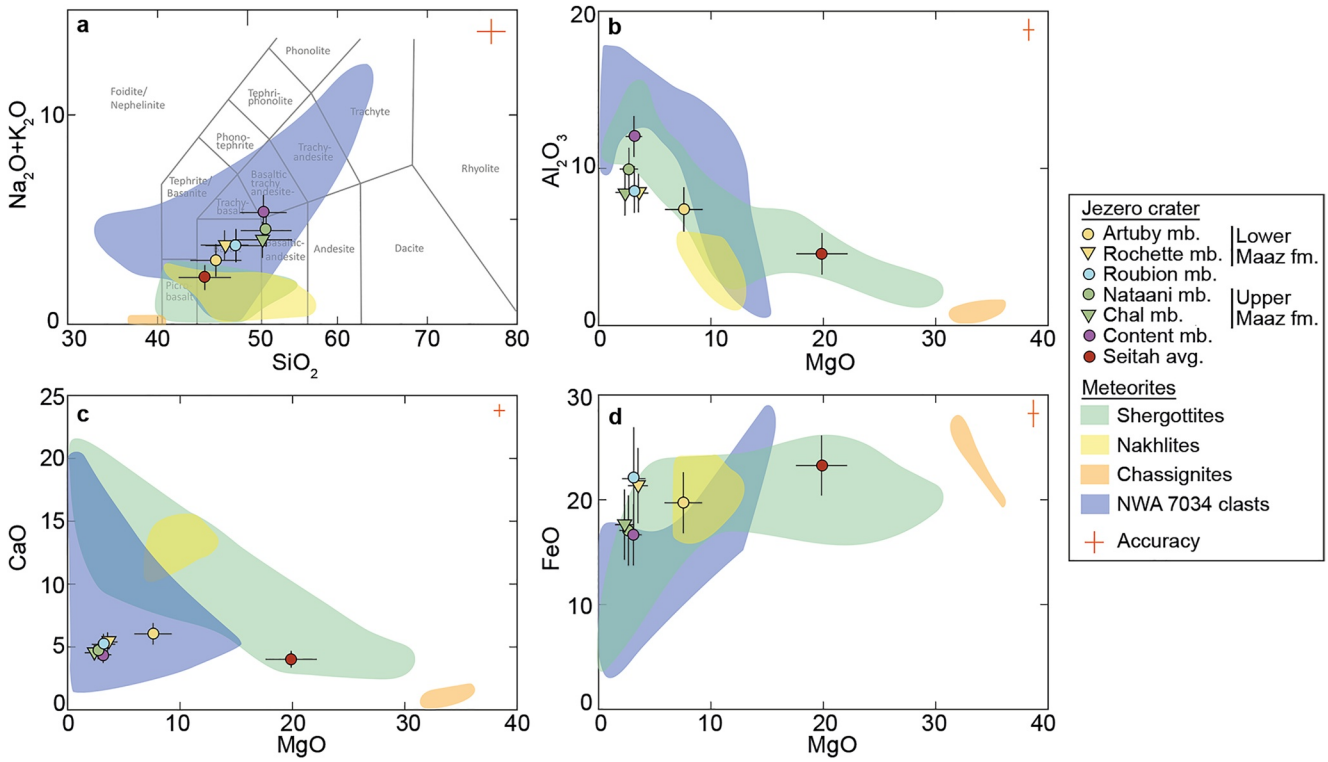

Figure 10. SuperCam Laser-Induced Breakdown Spectroscopy (LIBS) averages of major cations in wt. % for natural uncoated rock surfaces in all crater floor members (Udry et al., 2022), compared to compositional fields for Mars meteorites (Udry et al., 2020).

contrast (Carli & Sgavetti, 2011; Carli et al., 2015; Scudder et al., 2021). However, this explanation cannot explain the breadth of the band. Mixed valence Fe-bearing phyllosilicates often exhibit a broad and asymmetric band centered near 1.1 μm that has been identified in deep weathering profiles on Mars (e.g., Bishop et al., 2013), and SuperCam VISIR spectra do detect weak Fe/Mg-OH bands near 2.3 μm that are consistent with low abundances of a phyllosilicate mixture (Mandon et al., 2023). While we cannot rule out a contribution from phyllosilicates, these alteration bands are weak compared to the broad 1.1–1.2 μm band and we do not observe them from orbit (Horgan et al., 2020a), suggesting that the 1.1–1.2 μm band is too strong to be explained by this type of minor alteration.

The broad 1.1–1.2 μm band also resembles the broad and complex band exhibited by some Ca-saturated and Fe-rich pyroxenes (e.g., $Wo_{51}Fs_{49}$ CPX in Figure 5b, Cloutis & Gaffey, 1991a; Horgan et al., 2014; Klima et al., 2011; Schade et al., 2004). This spectral type of pyroxene ("Type A") occurs when other cations prevent Fe^{2+} from occupying both possible octahedral cation sites, and thus tends to correlate with high abundances of Ca^{2+} (>~Wo_{45}). The broad band is modeled as a triplet of bands around ~0.94, ~1.03, and 1.15 μm, with variable depths that lead to complex and variable spectral shapes (Schade et al., 2004). While the Maaz formation does appear to contain significant Ca-rich pyroxenes, it is unclear whether or not these are Ca-saturated.

Finally, the ~1.1 μm band could be due to coarse Fe-bearing feldspar crystals, or a mixture of coarse feldspar with pyroxene. Pure feldspars do not exhibit diagnostic absorption bands at VNIR/SWIR wavelengths, but substitution of even small amounts of Fe^{2+} results in a broad and shallow band centered between 1.1 and 1.3 μm, and most plagioclases more sodic than An_{50} contain sufficient iron to exhibit this band (Adams & Goullaud, 1978). This band is not usually apparent in igneous rocks, as plagioclase is relatively transparent compared to mafic minerals, and thus even >5%–25% olivine or pyroxene is sufficient to obscure this band (Cheek & Pieters, 2014; Serventi et al., 2013). However, laboratory studies have shown that mixtures of coarse plagioclase grains and Type A pyroxene are still dominated by plagioclase even in a 1:1 mixture (Rogers & Nekvasil, 2015), perhaps due to both the relatively low spectral contrast in this spectral type of pyroxene and the large grain size of the plagioclase. This may be similar to the Chal and Nataani members, which both have ~1:1 mixtures of plagioclase and pyroxene and exhibit coarse plagioclase crystal laths in the Alfalfa abrasion patch (Figure 8a).

Thus, we hypothesize that the VNIR/SWIR spectral signature of the Chal and Nataani members is due to a combination of coarse plagioclase and Ca-saturated pyroxene. CRISM spectra of rough hummocky and smooth polygonally fractured terrains also show a weak band near 860 nm consistent with hematite, which is consistent with Mastcam-Z spectra of the natural surfaces of the Chal and Nataani members (and to a lesser degree, the Roubion member) that are dominated by hematite mixed with some pyroxene (green in Figure 7).

CRISM spectra of smooth areas near outcrops of the Rochette and Artuby members (dark blue spectra in Figure 5a) have some qualities that resemble the Chal and Nataani members, including a broad band between 700 and 1,700 nm and a strong downturn at longer wavelengths. However, the broad band is centered at shorter wavelengths, closer to 1,000 nm, and the smooth areas also show an additional upturn near 2,500 nm that we attribute to the long edge of the HCP ∼2,000 nm band, which is not observed in any of the average SuperCam bedrock spectra. Instead, both SuperCam and CRISM spectra of fine regolith on the crater floor show broad absorptions centered near 1,000 and 2,100 nm consistent with HCP (Mandon et al., 2023), suggesting that regolith is contributing to the CRISM signature (Mandon et al., 2023; Vaughan et al., 2023). Thus, we hypothesize that the typical spectrum of the smooth areas is a mixture of Rochette and Artuby member bedrock (i.e., broadly similar to the Chal and Nataani members; green spectra in Figure 5a) and fine regolith (light blue spectrum in Figure 5a).

The Maaz formation may be a source for at least some of the local fine regolith (Vaughan et al., 2023). Mastcam-Z spectra of fine-grained regolith exhibit a broad band centered >900 nm consistent with pyroxene, and similar weak bands are found in Mastcam-Z spectra of abrasion patches throughout the Maaz formation. However, this band most strongly dominates the natural surface of the Rochette member (red/magenta in Figure 7). SuperCam also reported the highest average CaO abundances at Artuby ridge (Rochette and Artuby members), which Wiens et al. (2022) attributed to higher CPX abundances. Thus, we hypothesize that Rochette and the compositionally similar but more friable Artuby member is a local source of CPX-dominated fine regolith, and this hypothesis is supported by CRISM observations of concentrations of this signature around the Rochette fractured block surface morphology.

5. Stratigraphy

Figure 11a shows the elevation of named and localized Maaz formation outcrop targets, with groupings corresponding to the type localities of each member. A simple stratigraphic relationship based on elevation alone would order the members from top to bottom as Chal, Nataani, Rochette, Artuby, and Roubion (Crumpler et al., 2023; Simon et al., 2023). However, this simple stratigraphic model does not account for the overall regional dip to the southeast that is visible between the two sets of Rochette member points in Figure 11a. It is also not clear that Roubion is the stratigraphically lowest member, as both the Roubion member as well as the Artuby and Rochette members appear to directly overlie the Seitah formation, the latter where the units are all clearly exposed at the base of the Artuby ridge (Figure 4f). The Nataani and Chal members are likely to be the stratigraphically highest, as they occupy the highest elevations in the area, but if this is the case, then the observation that neither the Nataani or Chal members are present on top of or to the south of Artuby ridge suggests that they have been eroded from or were never deposited in this area. These observations suggest that the stratigraphy of the crater floor could be quite complex and that a simple elevation-based model may not be correct.

The relationship between the Nataani and Chal members and the Artuby and Rochette members is also not well understood, as no unambiguous contact between the two sets of members was identified close to the traverse. In addition, the Roubion member appears to underlie the Nataani member in the region of Polygon Valley (Section 3.2), but its distribution outside of this area is unclear, so the relationship between the Roubion member and the Artuby and Rochette members is also unknown. While Perseverance passed by several key outcrops that could help constrain the stratigraphy, their distance from the rover makes morphologic interpretations more challenging and ambiguous. Here we use multispectral landscape views to help inform stratigraphic interpretations of distant outcrops, and integrate RIMFAX subsurface soundings to build the local stratigraphic models shown in Figures 11b–11d.

5.1. Mastcam-Z Multispectral Landscape Views

As with the abrasion patches, we find that the "mafic" parameter color combination described in Section 4.2 (Figure 7) is helpful for discriminating between Maaz members in landscape and outcrop. Chal and Nataani both

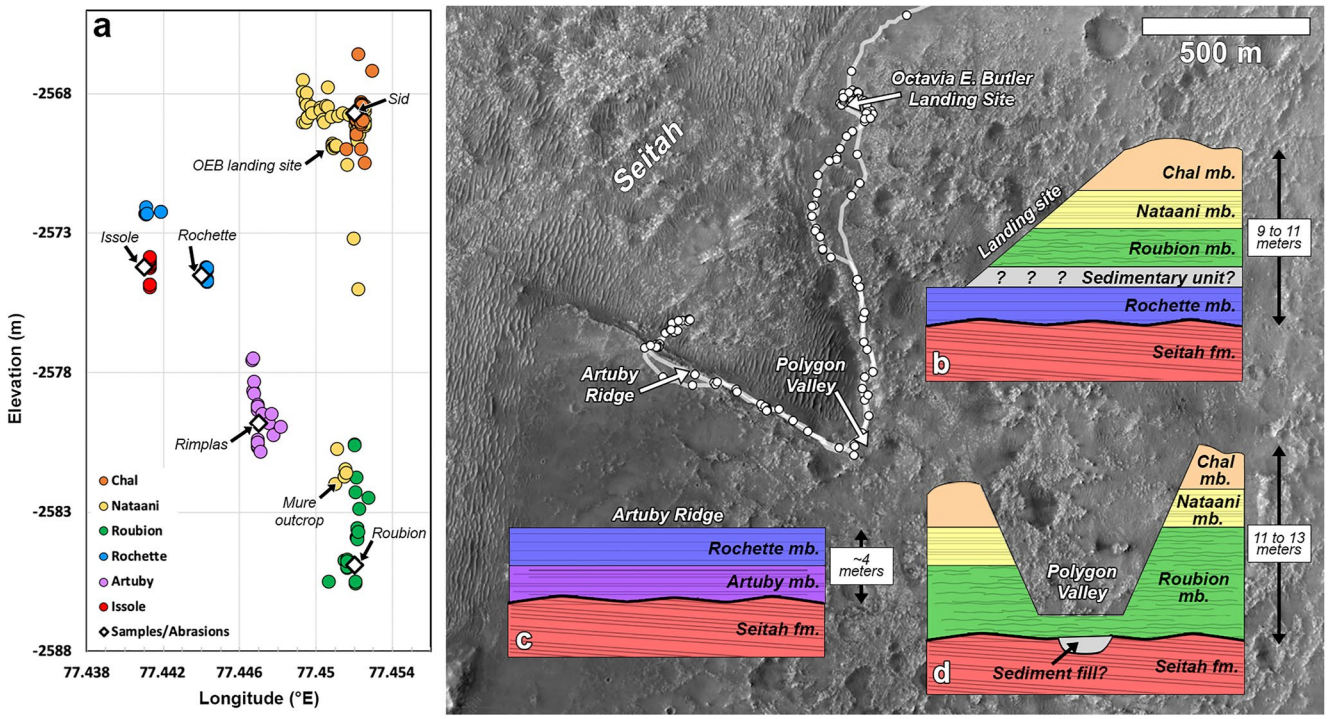

Figure 11. Stratigraphy of the crater floor. (a) Approximate elevation of named and localized targets from each member of the Maaz formation, along with the Issole outcrop (within the Seitah formation) at the base of Artuby ridge, and relevant samples and abrasion sites (labeled with rock name). (b–d) Interpreted local stratigraphic models for the crater floor, based on relationships in outcrop and ground penetrating radar (GPR) data, near (b) the landing site, (c) Artuby ridge, and (d) Polygon Valley (see Section 3.2 for discussion of Roubion member thickness), as shown in background HiRISE mosaic (Figure 1c). These models are simplifications of the stratigraphy and do not make predictions for local or regional dips.

appear as green and the Roubion member shows up as magenta. The most resistant layers in the Rochette member are distinctly red, while more recessive underlying layers are more magenta, and Artuby shows small-scale mixing between magenta and blue. These multispectral parameters are helpful for assisting in member identification, but are most appropriate when used in parallel with morphologic assessments, as they are subject to modification by factors like dust, coatings, and variable illumination geometries. Dusty and purple coated surfaces look weakly green because they have very low values for the slope parameters in the red and blue channels and weak BD910 values in the green channel. However, a continuous green color correlated with dark rock surfaces is likely due to rock properties.

To develop a more comprehensive stratigraphy, we first focus on the landing site, where the Nataani and Chal members are clearly present. If they are stratigraphically higher than the Rochette and Artuby members, we may expect these units to be present in the area at lower elevations. And indeed, a Rochette-like resistant and blocky cap forms the margin of the Maaz formation to the west of the landing site (Figure 12a). While this outcrop was not visited by the rover, the cap rock appears bright red in our Mastcam-Z "mafic" parameter combination, consistent with the Rochette member, and shows Rochette-like spectra, suggesting that this is the northern equivalent of the Rochette member. This observation supports our first-order interpretation that the Chal and Nataani members postdate the Rochette and Artuby members.

To the south of this outcrop, the Rochette-like margin is overlain by rough, pitted, dark, and layered blocks similar to Roubion, with a magenta color in the Mastcam-Z "mafic" RGB also consistent with Roubion (Figure 12b). Above this area, a higher ridge exhibits massive layers. These layers are at elevations consistent with Nataani, with the green color in the Mastcam-Z "mafic" RGB expected for Nataani. The flat terrain to the east of these outcrops is dominated by the Nataani member, which transitions to the Chal member further east. This suggests a relatively simple stratigraphy near the landing site of Rochette overlain by Roubion, Nataani, and then Chal (Figure 11b). Outcrops consistent with Artuby were not apparent in rover views of this area, and thus are either not present or obscured by regolith.

10.1029/2022JE007612

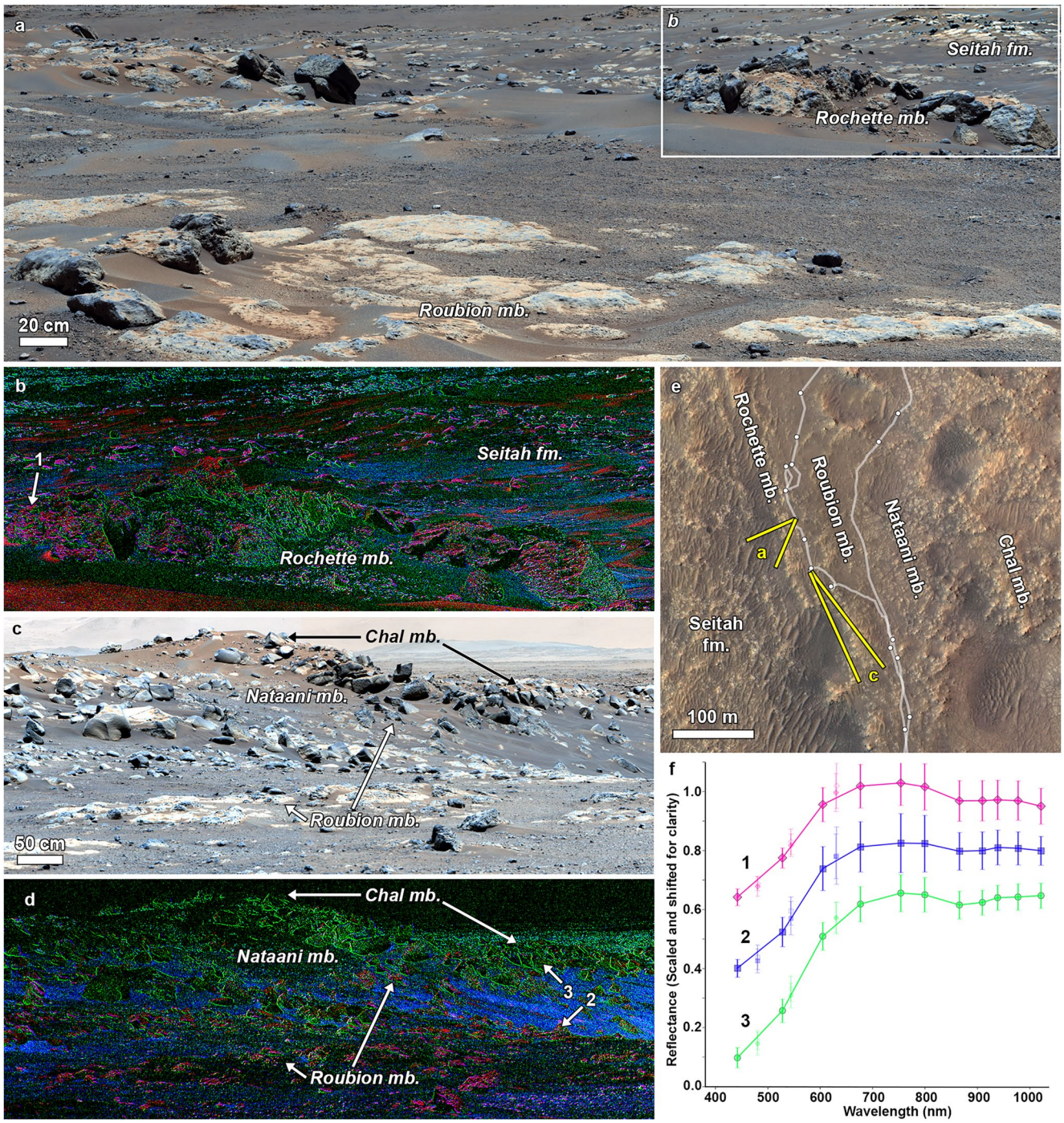

Figure 12. Outcrops at the margin of the Maaz formation west of the landing site. (a) Dark and pitted paver forming rocks consistent with the Roubion member transition to massive pitted blocks consistent with the Rochette member at the western edge scarp of the Maaz formation, overlooking Seitah (sol 124 zcam08121). (b) Multispectral mafic parameter combination similar to Figure 7, where magenta/red corresponds to additional reflectance near 650 nm typical of Rochette and Roubion member rocks (spectrum from point 1 shown in panel (f); sol 124 zcam03170). (c) The Roubion plateau is overlain by Nataani and Chal member outcrops on the margin of a small impact crater cut into the Maaz western scarp (sol 129 zcam03173), where morphological interpretations are supported by (d) the mafic parameter combination. (e) HiRISE color mosaic context map showing approximate viewsheds for (a–d). (f) Plot of spectra from locations numbered in panels (b, d).

5.2. RIMFAX Subsurface Soundings

RIMFAX subsurface soundings support our interpretation of the stratigraphy near the landing site based on surface outcrops (Figure 13a). Near the western margin of Maaz and the outcrops in Figure 12, the Maaz formation appears to be 3–4 m thick, overlying the Seitah formation. Within this section, at least three distinct radar units can be identified above the Seitah formation. The lowermost unit is ∼2 m thick and shows strong blocky reflectors at its top surface, consistent with the radar profile of the Rochette member on Artuby ridge (Figure 13b) and supporting the interpretation of the Rochette member outcropping along the margin in Figure 12a. The middle unit is a radar relatively "transparent" zone ∼1 m thick, suggesting a low density and/or fine grained material. This unit is overlain by a subtly layered top unit, 1–2 m thick. Considering the Maaz formation members identified in outcrop nearby, one interpretation is that the middle unit is the Roubion member and the top unit is the Nataani member, likely with some regolith cover. However, the Roubion member is exposed at the surface in this area and tends to exhibit rough layering at smaller scales than the Nataani member, and so would be unlikely to be radar transparent. Thus, it is more likely that the Rochette member is overlain by a localized low-density sedimentary unit, and that the top unit is the Roubion member.

Moving south into Polygon Valley (Figure 13b), RIMFAX data show that the Roubion member at the surface appears to be directly overlying dipping beds of the Seitah formation, at about 1 m depth. The Rochette and Artuby members are not present, suggesting that they were either never present in this location or that they were eroded prior to the emplacement of the Roubion member. Given that this area appears to be a zone of erosion, we favor the latter interpretation. Indeed, a U-shaped radar transparent zone is present below the Roubion member in the center of Polygon Valley, potentially due to a sediment-filled erosional trough that pre-dated emplacement of the Roubion member, supporting this hypothesis. Thus, the only place where the Artuby member is clearly present around the southern or eastern margin of Seitah is along Artuby ridge (Figure 13c), perhaps suggesting a different emplacement and/or erosion history compared to the Rochette member.

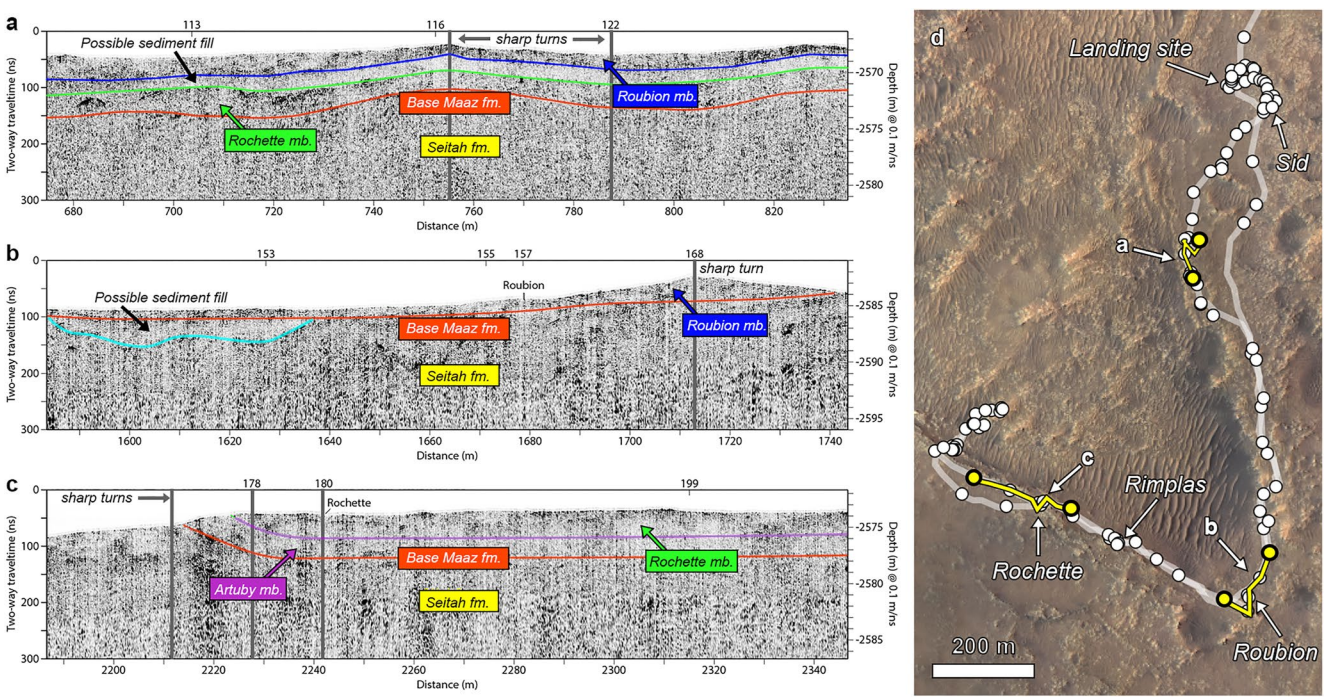

Figure 13. Radar Imager for Mars' subsurface eXperiment (RIMFAX) profiles along key stratigraphic intervals in the Maaz formation, source radargrams shown in Figure S2 in Supporting Information S1. (a) Subsurface reflections near the western margin (sols 112–123) show several distinct units, including a unit with strong upper surface reflections that we interpret as the Rochette member and a transparent unit that we interpret as a low-density fill such as sediments. The Artuby member is not apparent in this area. Note the double-back of the route, centered on sol 116, resulting in similar sections to the left and right of 116 label in the radargram. (b) Polygon Valley (sols 152–169) shows a thin (∼1 m) layer of Maaz formation rocks that correspond to weathered Roubion member at the surface, overlying dipping beds of the Seitah formation. The Rochette and Artuby members are not apparent in this area. (c) The rover traverse up to and along Artuby ridge (sols 177–200) shows that the Maaz formation (Artuby and Rochette members) dips away from the Seitah formation near the margin. The layers flatten out after sol 180 where the rover took a 90° turn to drive along the ridge. (d) HiRISE color context map showing locations of drive segments in panels (a–c).

5.3. Stratigraphic Models

The outcrop properties of the Maaz formation are consistent with a stratigraphic sequence from top to bottom of Chal, Nataani, Roubion, Rochette, and Artuby members, all overlying the Seitah formation (Figures 11b–11d). However, the dips and strikes of the members and their variability is not well constrained from this analysis and would require further detailed study, for example, using 3D models derived from stereo imaging and RIMFAX profiles. In addition, the different members have distinct distributions, as the Artuby member is not detected outside of Artuby ridge. The Rochette member is not detected in the area of Polygon Valley, suggesting that if it was once continuous, that it must have undergone significant erosion prior to the emplacement of the Roubion member. Interestingly, the Roubion member is underlain by lenses or layers of radar transparent materials at both the landing site and in Polygon Valley, possibly indicating sediments and supporting a period of erosion before it was emplaced. While most members appear to be on the order of 2 m thick, the Roubion member appears to be of highly variable thickness, ranging from 2 m near the landing site up to 7 m in parts of Polygon Valley, suggesting deposition on significant topography.

6. Discussion

6.1. Similarities and Differences Between Members of the Maaz Formation

Based on orbital and in situ morphology and spectral properties as well as in situ composition, we can broadly divide the Maaz formation along the rover traverse into two distinct groups, referred to here as the upper and lower Maaz formation. This could be due to the presence of two distinct series of lava flows that may have different emplacement histories and timing. This interpretation is consistent with Wiens et al. (2022), who first proposed a similar split based on LIBS compositional differences.

The lower Maaz formation includes the Artuby and Rochette members, and as a group is represented by the Montdenier and Montagnac samples from the Rochette member. The lower Maaz formation exhibits mafic (basaltic) bulk chemistries, relatively unoxidized natural surfaces with weak HCP signatures in Mastcam-Z data, and outcrop expressions dominated by thin layers or planar joints. The two members do exhibit somewhat distinct morphological and spectral properties, so they may have experienced different emplacement or modification histories. In particular, while a lava flow origin is strongly supported for the Rochette member (Crumpler et al., 2023; Simon et al., 2023), a pyroclastic origin has not been ruled out for the Artuby member (Alwmark et al., 2023), as the thin (cm-scale) and friable layers or foliations characteristic of the Artuby member are uncommon in terrestrial lava flows. If the Artuby member was composed of pyroclastic deposits, the chemical similarity to the Rochette member would be consistent with a similar volcanic source (Udry et al., 2022).

The upper Maaz formation includes the Chal and Nataani members, and as a group is represented by the Hahonih and Atsah samples from near the boundary between the Chal and Nataani members. The upper Maaz formation exhibits bulk chemistries that are less primitive and more enriched in SiO_2 (basalt to basaltic-andesite, Udry et al., 2022; Wiens et al., 2022) than the lower Maaz formation, variable hematite, pyroxene, or mixed signatures on their natural surfaces in Mastcam-Z data, massive morphologies, and textures consistent with lava flows. The primary difference between the Chal and Nataani members appears to be the smooth and terraced top surface, vesicle trains, and thick planar to lobate layers of the Nataani member compared to the massive, hummocky, and boulder-producing morphology of the Chal member. These differences are consistent with variable lava flow morphologies, where the Nataani member may have been emplaced as layers of pāhoehoe, while the Chal member may have been one or more thick a'a flows (Crumpler et al., 2023). The Nataani member shows evidence for spheroidal weathering, consistent with a weathering horizon at the top of the Nataani member (Crumpler et al., 2023), and suggesting that some time may have elapsed before emplacement of the Chal member.

Based on the stratigraphy presented here, Roubion is stratigraphically intermediate between the upper and lower Maaz formation and may be transitional. While its average bulk chemistry, dark pitted texture, and layered or foliated outcrop expression are more similar to the lower Maaz formation, Roubion has a distribution that is much more similar to the upper Maaz formation, and also shows surface oxidation that is characteristic of the upper Maaz formation. The presence of possible sedimentary layers beneath Roubion also suggests that some time passed between the lower Maaz formation and emplacement of the Roubion member.

The Content member of the Seitah formation is a pitted olivine-poor unit that drapes the Bastide ridge sampled by Perseverance in Seitah (Beyssac et al., 2023). Compositionally, the Content member is chemically similar to the

upper Maaz formation (and even a little more Al-enriched, Udry et al., 2022), and thus could be a related igneous unit. For example, given the draping nature of the Content member, an origin as a late tephra deposit or lava flow from the same source as the upper Maaz formation is plausible.

6.2. Extent of the Maaz Formation on the Crater Floor

From orbit (Figure 14), the lower Maaz formation appears to be associated with relatively smooth regolith-dominated surfaces with fragmented blocks, and we hypothesize that these form due to the thinly layered nature of both members and perhaps also due to the fissile, granular, and thus recessive nature of the Artuby member. These recessive properties likely lead to poor crater preservation in these areas. The CRISM HCP signatures that dominate these areas are likely due to regolith that we hypothesize is sourced from these members based on their similar spectral properties. The area southwest of Artuby ridge exhibits low thermal inertia values consistent with regolith cover (Figure 14d).

Several observations suggest that the lower Maaz formation extends beyond the area of the crater floor campaign. A distinct region toward the middle of the crater floor exhibits similar spectral, textural, and thermal inertia properties as the lower Maaz formation, and could either be a continuation of these members or unrelated regolith cover (Figure 14b). Furthermore, we hypothesize that because the more resistant layers of the Rochette member define the sharp margins of the Maaz formation near Seitah, that they (or similar strata) could be responsible for the lobate margins that characterize much of the crater floor more generally (Figure 1a).

We hypothesize that the lower Maaz formation may also be the primary crater floor rocks underlying the delta. The Maaz formation near the delta is largely obscured by thick regolith, but exhibits lobate margins similar to Artuby ridge and a surface texture similar to that observed south of Artuby ridge. In some locations, this area exhibits OPX absorptions in CRISM data similar to the delta top, and thus consistent with erosion from the delta or previously overlying sediments (Holm-Alwmark et al., 2021). However, the overall spectral signature in the area is most consistent with a mixture of OPX with CPX, which could suggest that the lower Maaz formation is the main substrate in the area.

While these interpretations suggest that the lower Maaz formation is widespread across the crater floor, the upper Maaz formation may be more localized. The upper Maaz formation is associated with rough textures and partially preserved craters, and we hypothesize that the CRISM signatures in the rough terrains to the east of the landing site are due to coarse feldspar and/or high-Ca pyroxene, as also observed most strongly in Mastcam-Z and SuperCam spectra of the upper Maaz formation. These properties extend across an area south and southeast of the landing site (dashed outline in Figure 14). To the south of Artuby ridge, upper Maaz forms a sharp boundary that could represent an erosional front. However, there is no evidence for Chal or Nataani-like materials west of this margin in any orbital data sets, so we instead interpret this as a possible original flow margin. Furthermore, no textures or spectral properties consistent with upper Maaz are observed north or west of the landing site. Together, these properties are consistent with emplacement of the upper Maaz formation as lava flows with a much more restricted extent across the crater floor than the lower Maaz formation. A variety of factors can influence lava flow area, flow paths, and spreading, including eruptive volume, substrate topography and roughness, and viscosity (e.g., Favalli et al., 2009; Richardson & Karlstrom, 2019; Rumpf et al., 2018). We hypothesize that the upper Maaz formation may have represented a smaller eruptive volume, possibly with higher viscosity, than the more extensive lower Maaz formation, and that the extent of the upper Maaz formation may have been controlled by paleotopography at the time of emplacement.

6.3. Possible Volcanic Sources

Several possible volcanic edifices are present in and around Jezero crater that could have been sources for the Maaz formation lavas. Jezero Mons is a very large conical edifice rising 2 km above the SE rim of Jezero crater that is most likely volcanic in origin (Figure 15a, Horgan et al., 2020a). While Jezero Mons is currently downslope from the Maaz formation, further careful analysis of the paleotopography and tectonic evolution of the area is required to rule it out as a lava flow source (see discussion of possible tectonic modification of the Maaz formation in the next section). Furthermore, any explosive eruptions at Jezero Mons would be expected to emplace tephra into Jezero crater (Ravanis et al., 2022). Similar but smaller steep-sided edifices are present to the southwest of Jezero crater (Figure 15e). Jezero Mons and these other edifices could represent a volcanic field,

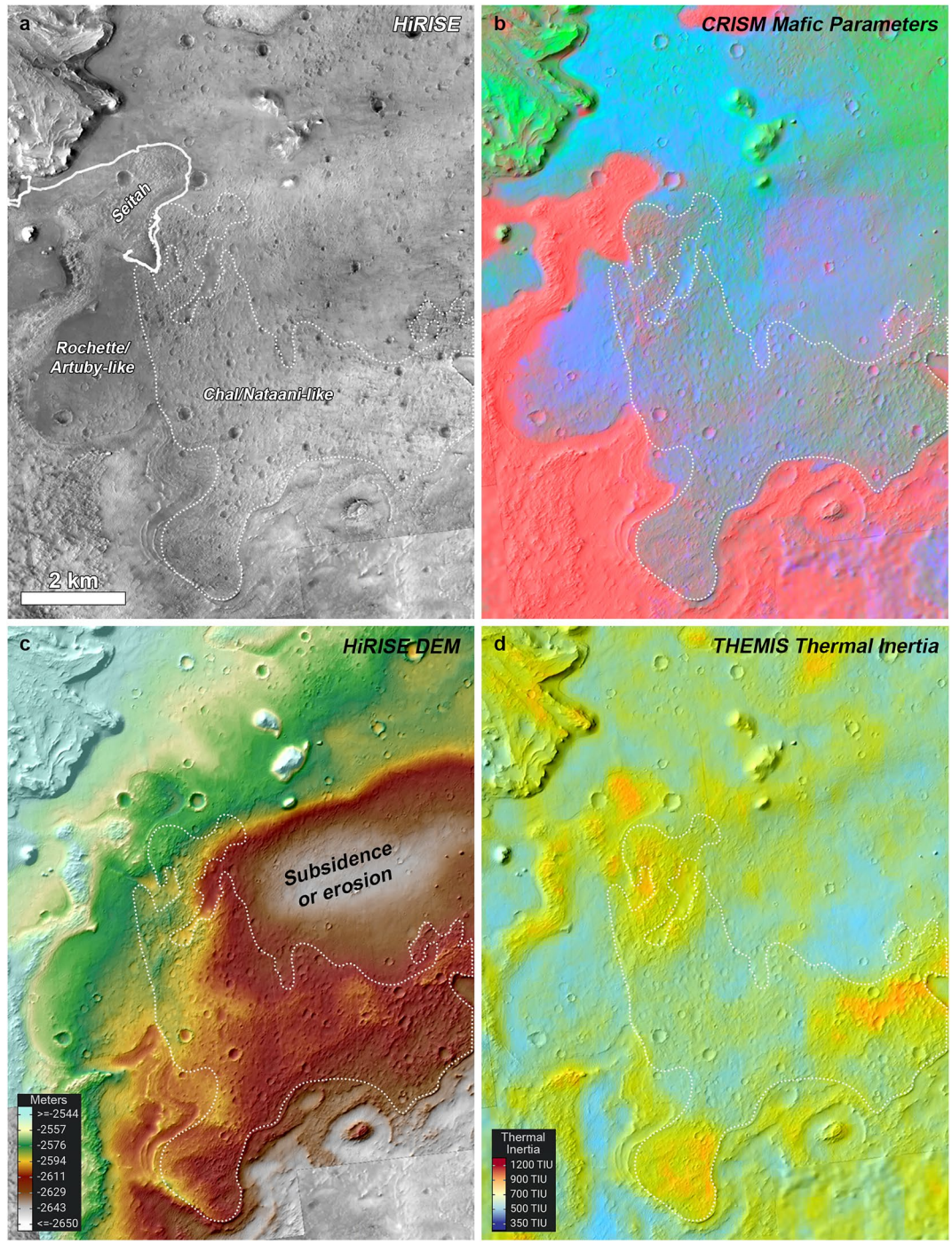

Figure 14. Inferred extent of Chal/Nataani-like surfaces (dashed line) on the southwestern crater floor near the landing site, based on orbital data sets. (a) High Resolution Imaging System (HiRISE) mosaic (Figure 1c), (b) Compact Reconnaissance Imaging Spectrometer for Mars mafic parameters color combination over Context camera (Figure 1b), (c) HiRISE elevation (Fergason et al., 2020), (d) Thermal Imaging System thermal inertia (Edwards & Buz, 2021), where (b–d) are all colorized over shaded relief from HiRISE (Fergason et al., 2020).

which would suggest significant regional volcanic activity in the past. Jezero crater itself contains a variety of mounds that could be volcanic, but are largely interpreted as slumped crustal blocks from the Jezero crater impact (Figure 15d, Sun & Stack, 2020). The most anomalous of these is a ~200 m high isolated edifice just inside the eroded northern rim of Jezero crater (Figure 15c). This northern edifice is the only volcano-like feature identified

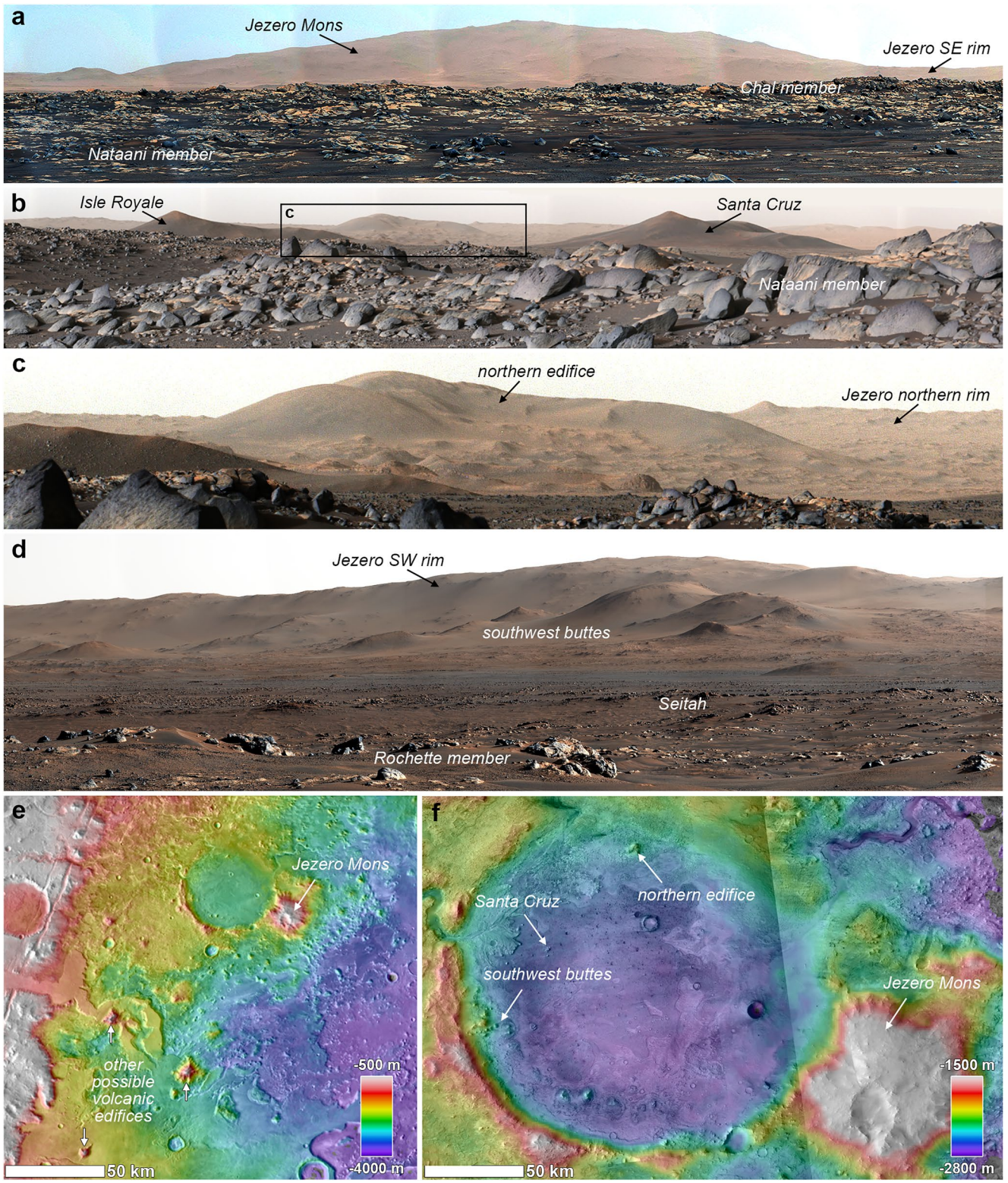

Figure 15. Mastcam-Z enhanced color views of possible volcanic features in and around Jezero crater. (a) Jezero Mons, approximately 40 km SE of the landing site and rising 2 km above the crater rim (sol 104, zcam08064). (b) Channel Islands buttes erosional sedimentary remnants, framing large edifice (~200 m high) inside northern rim, zoom shown in panel (c) (sol 353, zcam08382). (d) Southwest buttes interpreted as crustal blocks from the Jezero impact (sol 128, zcam08129). (e) Regional topographic context showing Jezero Mons and smaller steep sided edifices to southwest, the largest of which with peak elevations above −500 m are indicated by arrows. (f) Jezero crater local topography showing Jezero Mons and features in panels (a–d). (e, f) Show blended Mars Orbiter Laser Altimeter/High-Resolution Stereo Camera over Thermal Imaging System daytime infrared global mosaics (produced in JMARS, Christensen et al., 2009).

so far that is upslope from the Maaz formation and thus is currently the most plausible source, if it is a volcanic vent.

6.4. Emplacement History of the Maaz Formation

The stratigraphically lowest visible unit in Jezero crater is the Seitah formation, which is interpreted as an olivine cumulate emplaced as a thick lava flow, lava lake, or intrusion (Farley et al., 2022; Liu et al., 2022; Wiens et al., 2022). Orbital data shows that Seitah-like materials are present throughout the Jezero crater floor and, along with the Maaz formation, obscure all underlying units (Goudge et al., 2015; Horgan et al., 2020a), so any origin must account for the high volumes necessary to fill the crater. Emplacement models that produce the coarse olivine grains observed in the Seitah formation typically require melt depths of tens or up to one hundred meters, and should produce a stratigraphy of olivine-poor cumulates overlying the olivine-rich cumulates observed in the Seitah formation (Liu et al., 2022). Early hypotheses for the relationship between the Seitah and Maaz formations suggested that the lower Maaz formation could represent the upper portion (Artuby member) and surface flow (Rochette member) of this melt body (Farley et al., 2022; Wiens et al., 2022). In situ, the Artuby member does display some morphological similarities to the Seitah formation, including variably massive versus layered/recessive outcrops, with bedding at similar scales. However, this may not be supported by the details of the mineralogy of the lower Maaz formation compared to Seitah, as well as the high bulk abundance of iron measured in all Maaz members, which suggest distinct magma sources (Udry et al., 2022). If the Artuby and/or Rochette members are not representative of the upper portion of the Seitah melt body, then the actual upper portion must have been largely removed by erosion.

Thus, following the emplacement of the Seitah formation, we hypothesize that a period of erosion created significant topography on the crater floor, including the ridges that make up Seitah today. Deposition of the Maaz formation on this paleosurface began with emplacement of the Artuby and Rochette members widely on the crater floor, most likely as lava flows that embayed Seitah (Farley et al., 2022; Wiens et al., 2022). Given that the Artuby member is not apparent beneath the Rochette member near the landing site, it may have either had a different initial distribution or undergone erosion prior to the emplacement of the Rochette member.

Evidence points to additional erosion of the crater floor after the emplacement of the Rochette member lavas. The lower Maaz formation is absent beneath the Roubion member in Polygon Valley, so if they were once continuous, they were eroded from this area prior to emplacement of the overlying units. This suggests that Polygon Valley has been a persistent site of erosion through time, perhaps related to the topography of Seitah and interactions with dominant winds blowing coarse sand through this area. In support of a period of erosion at this time, the Roubion member appears to be underlain by radar transparent zones consistent with fine-grained sedimentary deposits both at the landing site and in Polygon Valley. These deposits were not observed in outcrop, so could be consistent with a variety of origins, including locally reworked materials, an aeolian deposit, or a fluviolacustrine deposit. The Roubion, Nataani, and Chal members were all emplaced as lava flows on this modified surface, once again embaying Seitah but also filling Polygon Valley.

The crater floor also shows evidence for other topographic modifications following emplacement of the lower Maaz formation, under the assumption that these members started out as flat lava flows: (a) local tilting of the lower Maaz formation along Artuby ridge to achieve local slopes ∼12° (Figure 13c), possibly due to uplift of Seitah by an unknown process (Hamran et al., 2022), (b) subsidence of Jezero basin fill creating an overall slope of ∼2°–3° toward the center of the basin (Figure 14c), (c) rebound of Isidis and Jezero basins, potentially producing complex regional tectonics. The evolution of the basin likely continued after the upper Maaz formation was emplaced as well, as these members also do not exhibit the constant topographic profile expected for a lava flow. However, some subsidence likely already occurred prior to emplacement of the upper Maaz formation, as one interpretation of the sharp margin on the upper Maaz formation south of Polygon Valley is that these flows embayed shallow slopes of the lower Maaz formation toward the delta.

Following emplacement of the Maaz formation, one or more periods of fluviolacustrine activity in Jezero crater created the western delta and likely covered the crater floor in 40 m or more of lake sediments, which are now preserved only in the rim of Hartwell crater to the northeast and within the Channel Islands buttes to the north of the landing site (Figure 15b, Quantin-Nataf et al., 2023). Some of the alteration observed within the Maaz formation could be related to this main period of lake activity, however, the presence of tens of meters of

fine-grained and impermeable lake sediments may have prevented significant infiltration of lake waters into the Maaz formation.

After cessation of lake activity, the lake sediments were eroded from the crater floor from east to west (the prevailing wind direction), gradually exposing the crater floor to impacts and producing a strong gradient in crater density increasing away from the delta (Quantin-Nataf et al., 2023). Additional weathering, erosion, and coating formation (Garczynski et al., 2022) shaped the crater floor that we observe today.

The biggest uncertainty in this model is the total time for emplacement of the Maaz formation, and in particular, the time between the emplacement of the lower Maaz formation and emplacement of the upper Maaz formation. The members of the Maaz formation all share similar mineralogy and geochemistry that could be consistent with a shared magma source, so a relatively short time for their overall emplacement is possible. But the erosion and other topographic modifications of the crater floor outlined above prior to emplacement of the Roubion, Nataani, and Chal members suggest that some significant time passed after emplacement of the Artuby and Rochette members. Furthermore, the Roubion member itself shows evidence for the development of a weathering profile, and spheroidal weathering has been tentatively identified on the Nataani member as well (Crumpler et al., 2023), possibly suggesting the presence of one or more weathered paleosurfaces within the Maaz stratigraphy and thus some significant time between flows.

As a result of these timing uncertainties, we cannot rule out that the upper Maaz formation could have been emplaced quite late in the history of Jezero crater, possibly even postdating lake activity and erosion of the sedimentary cover. While the lower Maaz formation appears to underlie the current delta and thus must predate fluviolacustrine activity, the upper Maaz formation does not underlie the delta or any sedimentary remnants on the floor and thus could postdate those deposits. Indeed, the upper Maaz formation could be absent near the delta because of the presence of partially eroded delta/lake sediments during their emplacement. Analysis of the alteration history of returned samples could help constrain the degree of aqueous interaction the lower versus upper Maaz formation experienced and thus their exposure to lake activity.

6.5. Relationship to Regional Units

The Seitah formation may be related to the regionally extensive Nilli Fossae olivine-bearing unit (Beyssac et al., 2023; Brown et al., 2020; Mandon et al., 2020; Wiens et al., 2022). The regional unit exhibits similar spectral signatures, production of coarse olivine sand grains, and fine-scale layering as the Seitah formation, but drapes underlying topography and thus may be more consistent with a tephra or other clastic deposit rather than an olivine cumulate or other effusive or intrusive deposit (Kremer et al., 2019). As such, it is unclear whether the Seitah formation cumulates and the regional unit are part of the same deposit, different volcanic deposits from the same magmatic edifice (e.g., explosive vs. effusive eruptions from the same vent), different volcanic deposits within a larger regional volcanic complex (e.g., from different vents fed by the same magma bodies or reservoirs), or totally different deposits (e.g., cumulate vs. aeolian deposit, Liu et al., 2022).

Likewise, the lower Maaz formation is spectrally and morphologically similar to the regional pyroxene-bearing Capping Unit (Hundal et al., 2022), which is an extensive cratered unit that drapes topography and thus is also interpreted as a tephra deposit. Notably, the capping unit always overlies the Seitah-like regional olivine/carbonate-bearing unit, suggesting a genetic link. In light of these observations, there may be a closer link between the Artuby member and the Seitah formation than is currently apparent from our in situ data. These regional units are major targets for Perseverance once the rover leaves Jezero crater to explore Nili Planum (Sun & Stack, 2020), so comparison of in situ data from the Capping Unit to the Maaz and Seitah formations will provide important context for the origin of the Jezero crater floor.

The upper Maaz formation does not have a clear relationship to previously identified regional units, but may provide insight into an enigmatic global class of rocks with potentially similar CRISM feldspar signatures (Carter & Poulet, 2013; Rogers & Farrand, 2022; Viviano-Beck et al., 2017; Wray et al., 2013). Some of these signatures have been attributed to coarse feldspar in basaltic to basaltic andesite lava flows (Rogers & Nekvasil, 2015), consistent with our observations of the upper Maaz formation, while others have been attributed to exposure of feldspar-rich lithologies (e.g., anorthosite, Phillips et al., 2022). A closer comparison of the upper Maaz formation to these other feldspar detections may help constrain their origin.

6.6. Geochronological Significance of Maaz Formation Samples

Geochronological analysis of Maaz formation samples after Mars Sample Return will help quantify the timeline described above, by quantifying any potential hiatus in the timing of crystallization between Rochette and Chal member samples. Crater densities suggest that the timescale of erosion of the lake sediments was on the order of hundreds of millions of years, at a minimum (Quantin-Nataf et al., 2023). For example, if the samples are close in age (say, within the precision of current analytical techniques for rocks billions of years in age, on the order of 10^5 or 10^6 years), this probably implies that all of the Maaz formation pre-dated lake activity, as described in the most likely timeline above, but separations of a hundred million years or more may suggest a more complex emplacement history.

The absolute crystallization ages of the Maaz formation samples will also be critical for addressing broader questions about the timing of major events in the Jezero region and possibly globally. The crystallization age of the Rochette member sample will place an important upper bound on the timing of fluvial activity in Jezero crater. Estimates for the main pulse of fluvial activity in the Jezero crater watershed have suggested a Late Noachian age consistent with the peak of global valley network activity (Fassett & Head, 2005), but more recent analyses have suggested that the lower portion of the watershed was reactivated at a later date, possibly in the Hesperian (Mangold et al., 2020). It is currently unclear which period of fluvial activity the bulk of the delta deposits were emplaced by (Mangold et al., 2021), but the age of Rochette member samples help constrain this by placing an upper bound on the timing of the delta.

In addition, the crystallization age of Chal member sample may help better constrain the martian cratering chronology, although the complex and extended exhumation history of the crater floor will make this connection challenging. Previous estimates for the age of the crater floor have included 1.4, $3.45 + 0.12/-0.67$, and 2.6 ± 0.5 Ga (Goudge et al., 2015; Schon et al., 2012; Shahrzad et al., 2019), where the range of ages is largely due to inclusion or exclusion of a small number of larger craters in the data set. More recently, Quantin-Nataf et al. (2023) showed that the strong gradient in crater density on the floor, which increases away from the delta, is consistent with gradual lateral exhumation of lake sediments on the crater floor toward the delta, resulting in higher crater densities in the floor units to the east that were exposed earlier. If a lateral progression in exhumation began >3 Ga and extended to present day, this scenario could predict an average crater retention age of ~2.5 Ga, which would be consistent with spatially averaged crater densities observed across the Jezero crater floor (Quantin-Nataf et al., 2023; Shahrzad et al., 2019). Results from our study further complicate the interpretation, as we postulate that different members within the Maaz formation also have very different crater retention properties.

However, from this study, the upper Maaz formation represents a rare example of a unit on the Jezero crater floor with well-defined boundaries and preserved craters, so more detailed analyses of its crater population along with knowledge of its crystallization age may shed light on the emplacement, burial, and exhumation history of the crater floor. Refinement of these models may provide constraints on the martian cratering chronology, especially if they can be supplemented by additional samples from other geochronological targets beyond the crater floor, most notably including the regional olivine/carbonate-bearing unit, which also has a well-defined crater retention age (Mandon et al., 2020). Additional samples from the rim of Jezero crater and megabreccia in the surrounding plains may also further aid in dating the Jezero and Isidis impacts, which would be important data points in the global cratering chronology.

7. Conclusions

The Jezero crater floor represents the first major geologic terrain investigated and sampled by the Perseverance rover, and samples from the Maaz formation on the crater floor will provide an important geochronological framework for the timing of events in Jezero crater. Lava flows are a key target for Mars Sample Return due to their high potential for investigations of their geochronology, petrology, and alteration history (Beaty et al., 2019). In this study, we found that the Maaz formation is consistent with a series of ancient lava flows, with different morphological expressions and spectral properties, which we have used to map their extent in orbital data. The Maaz formation can generally be split into two groups of members based on outcrop expression, spectral properties, composition, and distribution. The lower Maaz formation (Artuby and Rochette members) is responsible for the smooth surfaces and lobate margins in orbital imagers, as well as HCP signatures in CRISM data, that are all common across the Jezero crater floor. In contrast, the upper Maaz formation (Chal and Nataani

members) exhibit rough surfaces in orbital images as well as a lack of pyroxene and possible feldspar signatures in CRISM data, which together can be mapped to a well-defined lava flow extending southeast from the landing site. The bulk composition of the Maaz formation evolved over time from highly mafic at the base to basaltic andesite at the top, and the overall similarity in mineralogy and composition across the Maaz formation is consistent with a shared and evolving magma source. However, the evolution of the Jezero crater floor through time was complex, and likely included episodes of erosion, tectonic modification, burial by lake sediments, weathering, and exhumation, that occurred both before and after emplacement of the Maaz formation as well as in between emplacement of the upper and lower Maaz formation. The two unique samples collected by Perseverance within the Maaz formation are representative of these upper and lower members, and will allow us to directly test models for the sequence of events in Jezero crater, including the onset of fluvial activity and the exhumation history of the crater floor.

Acknowledgments
We would like to thank all members of the Mars 2020 science, operations, and engineering teams who made this paper possible, with special thanks to Justin Maki, Bethany Ehlmann, and Kevin Hand. The authors are especially grateful to the Mastcam-Z, SuperCam, and RIMFAX operations teams for their investment in the mission. We would also like to thank Christopher Hamilton and Christina Viviano for reviews that significantly improved the clarity of this paper. BH, MR, BG, JB, JJ, JN, CM, MSC, ER, and SF were funded by NASA's Mars 2020 Project via a subcontract from the California Institute of Technology/Jet Propulsion Laboratory to Arizona State University (Subcontract 1511125). The NASA Mars 2020 Participating Scientist program funded AU (80NSSC21K0330), LC (80NSSC21K0327), and NT. SA and TB were funded by the Swedish Research Council (Grant 2017-06388). HA and SEH were funded by the Research Council of Norway (Grant 309835 and 301238). KK was supported by the Carlsberg Foundation (Grant CF19-0023). LM was supported by CNES, CNRS, and IRIS OCAV. MM was supported by the EU's Horizon 2020 research and innovation programme under the Marie Skłodowska-Curie Grant (801199). JS, BC, and DS were funded by the NASA Return Sample Science Participating Scientist Program. AV was funded by NASA (Agreement 80HQTR20T0096). AB and GP were funded by ESA PRODEX Contract (PEA 4000117520). EC was funded by the Canadian Space Agency (Grant 22EXPCO14) and the Natural Sciences and Engineering Research Council of Canada (Grant RGPIN-2021-02995). DF was funded by the Australian Research Council (Grant DE210100205). SG was funded by the Royal Society Leverhulme Trust Senior Research Fellowship (SRF\R1\21000106) and the UK Space Agency (Grants ST/X002373/1 and ST/S001492/1). KS, YL, VS, and SS carried out their research contribution at the Jet Propulsion Laboratory, California Institute of Technology, under a contract with the National Aeronautics and Space Administration (80NM0018D0004). CQN was supported by CNES.

Data Availability Statement

The data in this publication are from the Mastcam-Z, RIMFAX, SuperCam, and SHERLOC/WATSON instruments on the Mars 2020 Perseverance rover, as well as data from the CRISM and HiRISE instruments on Mars Reconnaissance Orbiter. All image data presented here from Mastcam-Z (Bell & Maki, 2021), SHERLOC/WATSON (Beegle, 2021), RIMFAX (Hamran & Paige, 2021), CRISM (Seelos, 2016), and HiRISE (McEwen, 2007) are available through the Planetary Data System Imaging Node (https://pds-imaging.jpl.nasa.gov/portal/mars2020_mission.html) and GeoSciences Node (https://pds-geosciences.wustl.edu/missions/mars2020/). The Mastcam-Z multispectral database from sols 0–380 is published in Rice et al. (2022b), which includes all Mastcam-Z spectra shown here. Software packages used for Mastcam-Z image processing, spectral extraction, and statistical analyses are part of the open source "marslab" suite by Million Concepts, LLC (St. Clair et al., 2022). The SuperCam major element oxide composition (MOC), total emissivity, and all raw data and processed calibrated data files are included in the Planetary Data System (Wiens & Maurice, 2021). SuperCam average chemistry data for the Maaz members is available in Udry et al. (2022).

References

Adams, J. B., & Goullaud, L. H. (1978). Plagioclase feldspars - visible and near infrared diffuse reflectance spectra as applied to remote sensing. In *Lunar and planetary science conference* (Vol. 9, pp. 2901–2909).

Alwmark, S., Horgan, B., Udry, A., Bechtold, A., Fagents, S., Ravanis, E., et al. (2023). Varied origins of Artuby signals complex series of geologic events in Jezero crater, Mars. *Journal of Geophysical Research: Planets*. https://doi.org/10.1029/2022JE007446

Beaty, D. W., Grady, M. M., McSween, H. Y., Sefton-Nash, E., Carrier, B. L., Altieri, F., et al. (2019). The potential science and engineering value of samples delivered to Earth by Mars sample return. *Meteoritics & Planetary Sciences*, *54*(3), 667–671. https://doi.org/10.1111/maps.13232

Beegle, L. (2021). Mars 2020 SHERLOC bundle [Dataset]. NASA Planetary Data System. https://doi.org/10.17189/1522643

Bell, J. F., III, & Maki, J. N. (2021). Mars 2020 mast camera zoom bundle, from Arizona State University Mastcam-Z instrument team, calibrated products [Dataset]. NASA Planetary Data System. https://doi.org/10.17189/Q3TS-C749

Bell, J. F., III, Maki, J. N., Alwmark, S., Ehlmann, B. L., Fagents, S. A., Grotzinger, J. P., et al. (2022). Geological, multispectral, and meteorological imaging results from the Mars 2020 Perseverance rover in Jezero crater. *Science Advances*, *8*(47), eabo4856. https://doi.org/10.1126/sciadv.abo4856

Bell, J. F., III, Maki, J. N., Mehall, G. L., Ravine, M. A., Caplinger, M. A., Bailey, Z. J., et al. (2021). The Mars 2020 perseverance rover mast camera zoom (Mastcam-Z) multispectral, stereoscopic imaging investigation. *Space Science Reviews*, *217*(1), 24. https://doi.org/10.1007/s11214-020-00755-x

Beyssac, O., Chide, B., Cousin, A., Ayoub, F., Bertrand, T., Forni, O., et al. (2023). Coarse-grained olivine-rich regolith at Jezero crater, Mars: Nature, source, and transport. In *54th lunar and plantetary science conference* (Vol. 54, p. 1727). https://doi.org/10.1029/2022JE007638

Bishop, J. L., Loizeau, D., McKeown, N. K., Saper, L., Dyar, M. D., Marais, D. J. D., et al. (2013). What the ancient phyllosilicates at Mawrth Vallis can tell us about possible habitability on early Mars. *Planetary and Space Science*, *86*, 130–149. https://doi.org/10.1016/j.pss.2013.05.006

Brown, A. J., Kah, L., Mandon, L., Wiens, R., Pinet, P., Clavé, E., et al. (2023). Properties of the Nili Fossae olivine-clay-carbonate lithology: Orbital and in situ at Séítah. *arXiv preprint*. https://doi.org/10.48550/arXiv.2206.13380

Brown, A. J., Viviano, C. E., & Goudge, T. A. (2020). Olivine-carbonate mineralogy of the Jezero crater region. *Journal of Geophysical Research: Planets*, *125*(3), e2019JE006011. https://doi.org/10.1029/2019je006011

Carli, C., Serventi, G., & Sgavetti, M. (2015). VNIR spectral characteristics of terrestrial igneous effusive rocks: Mineralogical composition and the influence of texture. *Geological Society, London, Special Publications*, *401*(1), 139–158. https://doi.org/10.1144/sp401.19

Carli, C., & Sgavetti, M. (2011). Spectral characteristics of rocks: Effects of composition and texture and implications for the interpretation of planet surface compositions. *Icarus*, *211*(2), 1034–1048. https://doi.org/10.1016/j.icarus.2010.11.008

Carter, J., & Poulet, F. (2013). Ancient plutonic processes on Mars inferred from the detection of possible anorthositic terrains. *Nature Geoscience*, *6*(12), 1008–1012. https://doi.org/10.1038/ngeo1995

Casademont, T. M., Hamran, S. E., Amundsen, H. E. F., Eide, S., Dypvik, H., Berger, T., & Russell, P. (2023). Dielectric permittivity and density of the shallow Martian subsurface in Jezero crater. *Journal of Geophysical Research: Planets*, *2678*, 1513. https://doi.org/10.1029/2022JE007598

Cheek, L. C., & Pieters, C. M. (2014). Reflectance spectroscopy of plagioclase-dominated mineral mixtures: Implications for characterizing lunar anorthosites remotely. *American Mineralogist*, *99*(10), 1871–1892. https://doi.org/10.2138/am-2014-4785

Christensen, P. R., Engle, E., Anwar, S., Dickenshied, S., Noss, D., Gorelick, N., & Weiss-Malik, M. (2009). JMARS – A planetary GIS. In *American geophysical union, fall meeting 2009* (p. IN22A-06).
Christensen, P. R., Jakosky, B. M., Kieffer, H. H., Malin, M. C., McSween, H. Y., Jr., Nealson, K., et al. (2004). The thermal emission imaging system (THEMIS) for the Mars 2001 Odyssey Mission. *Space Science Reviews*, *110*(1/2), 85–130. https://doi.org/10.1023/b:spac.0000021008.16305.94
Cloutis, E. A., & Gaffey, M. J. (1991a). Pyroxene spectroscopy revisited: Spectral-compositional correlations and relationship to geothermometry. *Journal of Geophysical Research*, *96*(E5), 22809. https://doi.org/10.1029/91je02512
Cloutis, E. A., & Gaffey, M. J. (1991b). Spectral-compositional variations in the constituent minerals of mafic and ultramafic assemblages and remote sensing implications. *Earth, Moon, and Planets*, *53*(1), 11–53. https://doi.org/10.1007/bf00116217
Crumpler, L., Horgan, B., Simon, J., Stack, K., Alwmark, S., Gilles, D., et al. (2023). In situ geologic mapping transect observations on the Jezero crater floor from perseverance rover. *Journal of Geophysical Research: Planets*. e2022JE007444. https://doi.org/10.1029/2022JE007444
Edwards, C. S., & Buz, J. (2021). THEMIS-derived thermal inertia of Jezero crater, Mars (version 1) [Dataset]. Zenodo. https://doi.org/10.5281/zenodo.4931348
Farley, K. A., Stack, K. M., Shuster, D. L., Horgan, B. H. N., Hurowitz, J. A., Tarnas, J. D., et al. (2022). Aqueously altered igneous rocks sampled on the floor of Jezero crater, Mars. *Science*, *377*(6614), eabo2196. https://doi.org/10.1126/science.abo2196
Farley, K. A., Williford, K. H., Stack, K. M., Bhartia, R., Chen, A., de la Torre, M., et al. (2020). Mars 2020 mission overview. *Space Science Reviews*, *216*(8), 1–41. https://doi.org/10.1007/s11214-020-00762-y
Fassett, C. I., & Head, J. W. (2005). Fluvial sedimentary deposits on Mars: Ancient deltas in a crater lake in the Nili Fossae region. *Geophysical Research Letters*, *32*(14), L14201. https://doi.org/10.1029/2005gl023456
Favalli, M., Mazzarini, F., Pareschi, M. T., & Boschi, E. (2009). Topographic control on lava flow paths at Mount Etna, Italy: Implications for hazard assessment. *Journal of Geophysical Research*, *114*(F1), F01019. https://doi.org/10.1029/2007JF000918
Fergason, R. L., Hare, T. M., Mayer, D. P., Galuszka, D. M., Redding, B. L., Smith, E. D., et al. (2020). Mars 2020 terrain relative navigation flight product generation: Digital terrain model and orthorectified image mosaics. In *51st lunar and planetary science conference* (p. 2020).
Garczynski, B., Bell, J. F., III, Horgan, B. H. N., Johnson, J. R., Rice, M. S., & Vaughan, A. (2022). Perseverance and the purple coating: A Mastcam-Z multispectral story. In *53rd lunar and planetary science conference* (p. 2346).
Goudge, T. A., Mustard, J. F., Head, J. W., Fassett, C. I., & Wiseman, S. M. (2015). Assessing the mineralogy of the watershed and fan deposits of the Jezero crater paleolake system, Mars. *Journal of Geophysical Research: Planets*, *120*(4), 775–808. https://doi.org/10.1002/2014je004782
Haber, J. T., Horgan, B., Fraeman, A. A., Johnson, J. R., Bell, J. F., Rice, M. S., et al. (2022). Mineralogy of a possible ancient lakeshore in the Sutton Island member of Mt. Sharp, Gale crater, Mars, from Mastcam multispectral images. *Journal of Geophysical Research: Planets*, *127*(10), e2022JE007357. https://doi.org/10.1029/2022JE007357
Hamran, S. E., & Paige, D. A. (2021). Mars 2020 RIMFAX bundle [Dataset]. NASA Planetary Data System. https://doi.org/10.17189/1522644
Hamran, S. E., Paige, D. A., Allwood, A., Amundsen, H. E., Berger, T., Brovoll, S., et al. (2022). Ground penetrating radar observations of subsurface structures in the floor of Jezero crater, Mars. *Science Advances*, *8*(34), eabp8564. https://doi.org/10.1126/sciadv.abp8564
Hamran, S. E., Paige, D. A., Amundsen, H. E. F., Berger, T., Brovoll, S., Carter, L., et al. (2020). Radar imager for Mars' subsurface experiment—RIMFAX. *Space Science Reviews*, *216*(8), 1–39. https://doi.org/10.1007/s11214-020-00740-4
Hayes, A. G., Corlies, P., Tate, C., Barrington, M., Bell, J. F., Maki, J. N., et al. (2021). Pre-flight calibration of the Mars 2020 rover Mastcam zoom (Mastcam-Z) multispectral, stereoscopic imager. *Space Science Reviews*, *217*(2), 1–95. https://doi.org/10.1007/s11214-021-00795-x
Heggy, E., Clifford, S. M., Grimm, R. E., Dinwiddie, C. L., Wyrick, D. Y., & Hill, B. E. (2006). Ground-penetrating radar sounding in mafic lava flows: Assessing attenuation and scattering losses in Mars-analog volcanic terrains. *Journal of Geophysical Research*, *111*(E6), E06S04. https://doi.org/10.1029/2005JE002589
Holm-Alwmark, S., Kinch, K. M., Hansen, M. D., Shahrzad, S., Svennevig, K., Abbey, W. J., et al. (2021). Stratigraphic relationships in Jezero crater, Mars: Constraints on the timing of fluvial-Lacustrine activity from orbital observations. *Journal of Geophysical Research: Planets*, *126*(7), e2021JE006840. https://doi.org/10.1029/2021je006840
Horgan, B. H. N., Anderson, R. B., Dromart, G., Amador, E. S., & Rice, M. S. (2020a). The mineral diversity of Jezero crater: Evidence for possible lacustrine carbonates on Mars. *Icarus*, *339*, 113526. https://doi.org/10.1016/j.icarus.2019.113526
Horgan, B. H. N., Cloutis, E. A., Mann, P., & Bell, J. F. (2014). Near-infrared spectra of ferrous mineral mixtures and methods for their identification in planetary surface spectra. *Icarus*, *234*, 132–154. https://doi.org/10.1016/j.icarus.2014.02.031
Horgan, B. H. N., Johnson, J. R., Fraeman, A. A., Rice, M. S., Seeger, C., Bell, J. F., et al. (2020b). Diagenesis of Vera Rubin ridge, gale crater, Mars, from Mastcam multispectral images. *Journal of Geophysical Research: Planets*, *125*(11), e2019JE006322. https://doi.org/10.1029/2019je006322
Hundal, C. B., Mustard, J. F., Kremer, C. H., Tarnas, J. D., & Pascuzzo, A. C. (2022). The circum-isidis capping unit: An extensive regional Ashfall deposit exposed in Jezero crater. *Geophysical Research Letters*, *49*(9), e2021GL096920. https://doi.org/10.1029/2021gl096920
Jaumann, R., Neukum, G., Behnke, T., Duxbury, T., Eichentopf, K., Flohrer, J., et al. (2007). The high-resolution stereo camera (HRSC) experiment on Mars express: Instrument aspects and experiment conduct from interplanetary cruise through the nominal mission. *Planetary and Space Science*, *55*(7–8), 928–952. https://doi.org/10.1016/j.pss.2006.12.003
Jol, H. M., & Bristow, C. S. (2003). GPR in sediments: Advice on data collection, basic processing and interpretation, a good practice guide. *Geological Society, London, Special Publications*, *211*(1), 9–27. https://doi.org/10.1144/gsl.sp.2001.211.01.02
Kinch, K. M., Madsen, M. B., Bell, J. F., Maki, J. N., Bailey, Z. J., Hayes, A. G., et al. (2020). Radiometric calibration targets for the Mastcam-Z camera on the Mars 2020 rover mission. *Space Science Reviews*, *216*(8), 1–51. https://doi.org/10.1007/s11214-020-00774-8
Klima, R. L., Dyar, M. D., & Pieters, C. M. (2011). Near-infrared spectra of clinopyroxenes: Effects of calcium content and crystal structure. *Meteoritics & Planetary Sciences*, *46*(3), 379–395. https://doi.org/10.1111/j.1945-5100.2010.01158.x
Kokaly, R. F., Clark, R. N., Swayze, G. A., Livo, K. E., Hoefen, T. M., Pearson, N. C., et al. (2017). USGS spectral library version 7: U.S. *Geological Survey Data Series*, *1035*, 61. https://doi.org/10.3133/ds1035
Kremer, C. H., Mustard, J. F., & Bramble, M. S. (2019). A widespread olivine-rich ash deposit on Mars. *Geology*, *47*(7), 677–681. https://doi.org/10.1130/g45563.1
Liu, Y., Tice, M. M., Schmidt, M. E., Treiman, A. H., Kizovski, T. V., Hurowitz, J. A., et al. (2022). An olivine cumulate outcrop on the floor of Jezero crater, Mars. *Science*, *377*(6614), 1513–1519. https://doi.org/10.1126/science.abo2756
Malin, M. C., Bell, J. F., Cantor, B. A., Caplinger, M. A., Calvin, W. M., Clancy, R. T., et al. (2007). Context camera investigation on board the Mars reconnaissance orbiter. *Journal of Geophysical Research*, *112*(E5), E05S04. https://doi.org/10.1029/2006JE002808
Mandon, L., Quantin-Nataf, C., Royer, C., Beck, P., Fouchet, T., Johnson, J. R., et al. (2023). Reflectance of Jezero crater floor: 2. Mineralogical interpretation. *Journal of Geophysical Research: Planets*. e2022JE007450. https://doi.org/10.1029/2022JE007450
Mandon, L., Quantin-Nataf, C., Thollot, P., Mangold, N., Lozac'h, L., Dromart, G., et al. (2020). Refining the age, emplacement and alteration scenarios of the olivine-rich unit in the Nili Fossae region, Mars. *Icarus*, *336*, 113436. https://doi.org/10.1016/j.icarus.2019.113436

Mangold, N., Dromart, G., Ansan, V., Salese, F., Kleinhans, M. G., Massé, M., et al. (2020). Fluvial regimes, morphometry, and age of Jezero crater paleolake inlet valleys and their exobiological significance for the 2020 Rover Mission Landing Site. *Astrobiology*, *20*(8), 994–1013. https://doi.org/10.1089/ast.2019.2132

Mangold, N., Gupta, S., Gasnault, O., Dromart, G., Tarnas, J. D., Sholes, S. F., et al. (2021). Perseverance rover reveals an ancient delta-lake system and flood deposits at Jezero crater, Mars. *Science*, *374*(6568), 711–717. https://doi.org/10.1126/science.abl4051

Maurice, S., Wiens, R. C., Bernardi, P., Caïs, P., Robinson, S., Nelson, T., et al. (2021). The SuperCam instrument suite on the Mars 2020 rover: Science objectives and mast-unit description. *Space Science Reviews*, *217*(3), 1–108. https://doi.org/10.1007/s11214-021-00807-w

McEwen, A. S. (2007). MRO Mars high-resolution imaging science experiment, reduced data record V1.1, MRO-M-HIRISE-3-RDR-V1.1 [Dataset]. NASA Planetary Data System. https://doi.org/10.17189/1520303

McEwen, A. S., Eliason, E. M., Bergstrom, J. W., Bridges, N. T., Hansen, C. J., Delamere, W. A., et al. (2007). Mars reconnaissance orbiter's high resolution imaging science experiment (HiRISE). *Journal of Geophysical Research*, *112*(E5), E05S02. https://doi.org/10.1029/2005je002605

Merusi, M., Kinch, K. B., Madsen, M. B., Bell, J. F., Maki, J. N., Hayes, A. G., et al. (2022). The Mastcam-Z radiometric calibration targets on NASA's perseverance rover: Derived irradiance time-series, dust deposition, and performance over the first 350 sols on Mars. *Journal of Geophysical Research: Planets*, *9*(12). e2022EA002552. https://doi.org/10.1029/2022EA002552

Milliken, R. (2020). RELAB spectral library bundle. *NASA Planetary Data System*. https://doi.org/10.17189/1519032

Minitti, M. E., Kennedy, M. R., Edgett, K. S., Beegle, L. W., Asher, S. A., Abbey, W. J., et al. (2021). The Mars 2020 Watson imaging subsystem of the SHERLOC investigation and anticipated early results. In *Lunar and planetary science conference* (p. 2028).

Moeller, R. C., Jandura, L., Rosette, K., Robinson, M., Samuels, J., Silverman, M., et al. (2021). The sampling and caching subsystem (SCS) for the scientific exploration of Jezero crater by the Mars 2020 perseverance rover. *Space Science Reviews*, *217*(1), 1–43. https://doi.org/10.1007/s11214-020-00783-7

Morris, R. V., Lawson, C. A., Gibson, E. K. J., Lauer, H. V. J., Nace, G. A., & Stewart, C. (1985). Spectral and other physicochemical properties of submicron powders of hematite (alpha-Fe_2O_3), maghemite (gamma-Fe_2O_3), magnetite (Fe_3O_4), goethite (alpha-FeOOH), and lepidocrocite (gamma-FeOOH). *Journal of Geophysical Research*, *90*(B4), 3126–3144. https://doi.org/10.1029/jb090ib04p03126

Murchie, S., Arvidson, R., Bedini, P., Beisser, K., Bibring, J.-P., Bishop, J., et al. (2007). Compact reconnaissance imaging spectrometer for Mars (CRISM) on Mars reconnaissance orbiter (MRO). *Journal of Geophysical Research*, *112*(E5), E05S03. https://doi.org/10.1029/2006je002682

Phillips, M. S., Viviano, C. E., Moersch, J. E., Rogers, A. D., McSween, H. Y., & Seelos, F. P. (2022). Extensive and ancient feldspathic crust detected across north Hellas rim, Mars: Possible implications for primary crust formation. *Geology*, *50*(10), 1182–1186. https://doi.org/10.1130/g50341.1

Quantin-Nataf, C., Alwmark, S., Calef, F. J., Lasue, J., Kinch, K., Stack, K. M., et al. (2023). The complex exhumation history of Jezero crater floor unit. *Journal of Geophysical Research: Planets*, *128*(6), e2022JE007628. https://doi.org/10.1029/2022je007628

Ravanis, E., Fagents, S., Newman, C., Horgan, B., Holm-Alwmark, S., Brown, A. J., et al. (2022). The potential for pyroclastic deposits in the Jezero crater region of Mars from ash dispersal modeling. In *53rd lunar and planetary science conference* (p. 1692).

Rice, M. S., Johnson, J. R., Million, C. C., St. Clair, M., Horgan, B. N., Vaughan, A., et al. (2022b). *Mastcam-Z multispectral database from the Perseverance rover's traverse in the Jezero crater floor, Mars (sols 0-380)* (Vol. 105). [Dataset]. WWU Geology Faculty Publications. https://doi.org/10.25710/bhyk-kc32

Rice, M. S., Johnson, J. R., Million, C. C., St. Clair, M., Horgan, B. N., Vaughan, A., et al. (2023). Spectral variability of rocks and soils on the Jezero crater floor: A summary of multispectral observations from Perseverance's Mastcam-Z instrument. *Journal of Geophysical Research: Planets*. e2022JE007548. https://doi.org/10.1029/2022JE007548

Rice, M. S., Seeger, C., Bell, J., Calef, F., St. Clair, M., Eng, A., et al. (2022a). Spectral diversity of rocks and soils in Mastcam observations along the Curiosity rover's traverse in Gale crater, Mars. *Journal of Geophysical Research: Planets*, *127*(8), e2021JE007134. https://doi.org/10.1029/2021je007134

Richardson, P., & Karlstrom, L. (2019). The multi-scale influence of topography on lava flow morphology. *Bulletin of Volcanology*, *81*(4), 21. https://doi.org/10.1007/s00445-019-1278-9

Rogers, A. D., & Farrand, W. H. (2022). Spectral evidence for alkaline rocks and compositional diversity among feldspathic light-toned terrains on Mars. *Icarus*, *376*, 114883. https://doi.org/10.1016/j.icarus.2022.114883

Rogers, A. D., & Nekvasil, H. (2015). Feldspathic rocks on Mars: Compositional constraints from infrared spectroscopy and possible formation mechanisms. *Geophysical Research Letters*, *42*(8), 2619–2626. https://doi.org/10.1002/2015gl063501

Rudolph, A., Horgan, B., Johnson, J., Bennett, K., Haber, J., Bell, J. F., et al. (2022). The distribution of clay minerals and their impact on diagenesis in Glen Torridon, Gale crater, Mars. *Journal of Geophysical Research: Planets*, *127*(10), e2021JE007098. https://doi.org/10.1029/2021je007098

Rumpf, M. E., Lev, E., & Wysocki, R. (2018). The influence of topographic roughness on lava flow emplacement. *Bulletin of Volcanology*, *80*(7), 63. https://doi.org/10.1007/s00445-018-1238-9

Schade, U., Wasch, R., & Moroz, L. (2004). Near-infrared reflectance spectroscopy of Ca-rich clinopyroxenes and prospects for remote spectral characterization of planetary surfaces. *Icarus*, *168*(1), 80–92. https://doi.org/10.1016/j.icarus.2003.10.016

Schon, S. C., Head, J. W., & Fassett, C. I. (2012). An overfilled lacustrine system and progradational delta in Jezero crater, Mars: Implications for Noachian climate. *Planetary and Space Science*, *67*(1), 28–45. https://doi.org/10.1016/j.pss.2012.02.003

Scudder, N. A., Horgan, B. H. N., Rampe, E. B., Smith, R. J., & Rutledge, A. M. (2021). The effects of magmatic evolution, crystallinity, and microtexture on the visible/near-infrared and thermal-infrared spectra of volcanic rocks. *Icarus*, *359*, 114344. https://doi.org/10.1016/j.icarus.2021.114344

Seelos, F. P. (2016). MRO CRISM Map-projected targeted reduced data record v1.0 [Dataset]. NASA Planetary Data System. https://doi.org/10.17189/1519470

Seelos, F. P., Viviano-Beck, C. E., Morgan, M. F., Romeo, G., Aiello, J. J., & Murchie, S. L. (2016). CRISM hyperspectral targeted observation PDS product sets—TERs and MTRDRs. In *47th lunar and planetary science conference* (p. 1783).

Serventi, G., Carli, C., Sgavetti, M., Ciarniello, M., Capaccioni, F., & Pedrazzi, G. (2013). Spectral variability of plagioclase–mafic mixtures (1): Effects of chemistry and modal abundance in reflectance spectra of rocks and mineral mixtures. *Icarus*, *226*(1), 282–298. https://doi.org/10.1016/j.icarus.2013.05.041

Shahrzad, S., Kinch, K. M., Goudge, T. A., Fassett, C. I., Needham, D. H., Quantin-Nataf, C., & Knudsen, C. P. (2019). Crater statistics on the dark-toned, mafic floor unit in Jezero crater, Mars. *Geophysical Research Letters*, *46*(5), 2408–2416. https://doi.org/10.1029/2018gl081402

Simon, J. I., Hickman-Lewis, K., Cohen, B. A., Mayhew, L. E., Shuster, D. L., Debaille, V., et al. (2023). Samples collected from the floor of Jezero crater with the Mars 2020 perseverance rover. *Journal of Geophysical Research: Planets*, *128*(6), e2022JE007474. https://doi.org/10.1029/2022JE007474

Stack, K. M., Williams, N. R., Calef, F., Sun, V. Z., Williford, K. H., Farley, K. A., et al. (2020). Photogeologic map of the perseverance rover field site in Jezero crater constructed by the Mars 2020 science team. *Space Science Reviews*, *216*(8), 127. https://doi.org/10.1007/s11214-020-00739-x

St. Clair, M., Million, C., & Rice, M. (2022). Marslab software suite [Software]. Retrieved from https://zenodo.org/badge/latestdoi/498892781

Sun, V. Z., Hand, K. P., Stack, K. M., Farley, K. A., Simon, J. I., Newman, C., et al. (2023). Exploring the Jezero crater floor: Summary and synthesis of Perseverance's first science campaign. *Journal of Geophysical Research: Planets*, *128*(6). https://doi.org/10.1029/2022JE007613

Sun, V. Z., & Stack, K. M. (2020). *Geologic map of Jezero crater and the Nili Planum region, Mars* (Vol. 3464). US Department of the Interior, US Geological Survey, Scientific Investigations Map.

Townsend, T. E. (1987). Discrimination of iron alteration minerals in visible and near-infrared reflectance data. *Journal of Geophysical Research*, *92*(B2), 1441–1454. https://doi.org/10.1029/jb092ib02p01441

Udry, A., Howarth, G. H., Herd, C. D. K., Day, J. M., Lapen, T. J., & Filiberto, J. (2020). What martian meteorites reveal about the interior and surface of Mars. https://doi.org/10.1029/2020JE006523

Udry, A., Ostwald, A., Sautter, V., Cousin, A., Beyssac, O., Forni, O., et al. (2022). A Mars 2020 perseverance SuperCam perspective on the igneous nature of the Máaz formation at Jezero crater, Mars. *Journal of Geophysical Research: Planets*. e2022JE007440. https://doi.org/10.1029/2022JE007440

Vaughan, A., Minitti, M. E., Cardarelli, E. L., Johnson, J. R., Kah, L. C., Pilleri, P., et al. (2023). Regolith of the crater floor units, Jezero crater, Mars: Textures, composition, and implications for provenance. *Journal of Geophysical Research: Planets*, *128*(3). e2022JE007437. https://doi.org/10.1029/2022JE007437

Viviano-Beck, C. E., Murchie, S. L., Beck, A. W., & Dohm, J. M. (2017). Compositional and structural constraints on the geologic history of eastern Tharsis Rise, Mars. *Icarus*, *284*, 43–58. https://doi.org/10.1016/j.icarus.2016.09.005

Viviano-Beck, C. E., Seelos, F. P., Murchie, S. L., Kahn, E. G., Seelos, K. D., Taylor, H. W., et al. (2014). Revised CRISM spectral parameters and summary products based on the currently detected mineral diversity on Mars. *Journal of Geophysical Research: Planets*, *119*(6), 1403–1431. https://doi.org/10.1002/2014je004627

Wiens, R. C., & Maurice, S. (2021). Mars 2020 SuperCam bundle. *NASA Planetary Data System*. https://doi.org/10.17189/1522646

Wiens, R. C., Maurice, S., Robinson, S. H., Nelson, A. E., Cais, P., Bernardi, P., et al. (2021). The SuperCam instrument suite on the NASA Mars 2020 rover: Body unit and combined system tests. *Space Science Reviews*, *217*, 1–87. https://doi.org/10.1007/s11214-020-00777-5

Wiens, R. C., Udry, A., Beyssac, O., Quantin-Nataf, C., Mangold, N., Cousin, A., et al. (2022). Compositionally and density stratified igneous terrain in Jezero crater, Mars. *Science Advances*, *8*(34), eabo3399. https://doi.org/10.1126/sciadv.abo3399

Wray, J. J., Hansen, S. T., Dufek, J., Swayze, G. A., Murchie, S. L., Seelos, F. P., et al. (2013). Prolonged magmatic activity on Mars inferred from the detection of felsic rocks. *Nature Geoscience*, *6*(12), 1013–1017. https://doi.org/10.1038/ngeo1994

Zuber, M. T., Smith, D. E., Solomon, S. C., Muhleman, D. O., Head, J. W., Garvin, J. B., et al. (1992). The Mars Observer laser altimeter investigation. *Journal of Geophysical Research*, *97*(E5), 7781–7797. https://doi.org/10.1029/92je00341